Marine and Petroleum Geology 153 (2023) 106253

Contents lists available at ScienceDirect

Marine and Petroleum Geology

journal homepage: www.elsevier.com/locate/marpetgeo

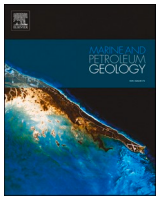

Geological controls on the distribution of gas hydrates in the shallow parts of the gas hydrate stability zone – constraints from seafloor drilling off Taiwan

G. Bohrmann [a,*], C. Berndt [b], S. Lin [c], T.-H. Tu [d], A.T. Lin [e], H.-H. Hsu [c], M.-C. Lai [f], W.-C. Chi [g], C. Deusner [b], J. Elger [b], K. Wallmann [b], T. Freudenthal [a], S. Mau [a], T. Pape [a], Y.-T. Tseng [a], P.-S. Yu [h], L.-F. Fan [c], J.-N. Chen [i], S.-C. Chen [f], T.-T. Chen [c], K.-Y. Wei [i], R/V SONNE SO266 shipboard scientific party

[a] MARUM – Center for Marine Environmental Sciences and Faculty of Geosciences, University of Bremen, Bremen, Germany
[b] GEOMAR Helmholtz-Zentrum für Ozeanforschung, Kiel, Germany
[c] Institute of Oceanography, National Taiwan University, Taipei, Taiwan
[d] Department of Oceanography, National Sun Yat-sen University, Kaohsiung, Taiwan
[e] Department of Earth Sciences and Carbon Storage and Geothermal Research Center, National Central University, Taoyuan, Taiwan
[f] Department of Life Sciences, National Chung Hsing University, Taichung, Taiwan
[g] Institute of Earth Sciences, Academia Sinica, Taipei, Taiwan
[h] Taiwan Ocean Research Institute, National Applied Research Laboratories, Kaohsiung, Taiwan
[i] Department of Geosciences, National Taiwan University, Taipei, Taiwan

ARTICLE INFO

Keywords:
Gas hydrate
Taiwan
Passive and active margin

ABSTRACT

The presence of gas hydrates is well known in the marine realm southwest of Taiwan due to the widespread distribution of bottom simulating reflectors in seismic records. To learn more about gas hydrate systems and their dynamics at passive and active margins, we drilled boreholes with MARUM-MeBo200 seafloor drill rig at areas where geophysical indications for gas hydrates have been detected in the past. Several gas hydrate proxies like negative chloride anomalies in the pore water, cold spots detected by infrared thermal scans on cores, increased resistivity, and lithological parameters clearly showed the presence of hydrates in the drilled sections. However, gas hydrate was not recovered by MeBo most likely because of small crystal sizes which dissociated during recovery from the seafloor. Three holes were drilled at southern summit of Formosa Ridge down to 126 m below seafloor (mbsf) and recovered sediments from which in situ hydrate saturation values were estimated between 1 and 10% at 15–42 mbsf and even higher values of up to 38% below 100 mbsf. The latter are probably related to the sealing effect of carbonate precipitation which occur at 85–95 mbsf directly above the hydrate-enriched layer. Four holes were drilled at Four-Way Closure Ridge where a maximum drilling depth of 143.90 mbsf was reached. Hydrate presence starts in 65 mbsf continuing down-core with a range of 1–29% gas hydrate saturation in fine-grained homogenous clay. An abrupt change to higher gas hydrate saturation values of up to 80% occurs below 109 mbsf where silty and sandy turbidite layers are often intercalated. Such high gas hydrate contents only occur in the sand layers and not in the fine-grained sediments intercalated to the sand deposits.

1. Introduction

Gas hydrates are crystalline solids, which are well known from marine sediments along the continental margins and from permafrost areas. Natural hydrate specimen look like ice, but in contrast to frozen water, methane hydrate is forming cage structures which is only possible when both methane and water molecules are available in excess. Water molecules form cages through hydrate bonds, and in each cage, there is space for one gas molecule. In natural hydrates, these so-called guest molecules predominantly consist of methane (CH_4), but other gases like ethane (C_2H_6), carbon dioxide (CO_2), hydrogen sulfide (H_2S), and many others can be involved [Sloan and Koh, 2008]. The presence of methane

* Corresponding author.
E-mail address: gbohrmann@marum.de (G. Bohrmann).

https://doi.org/10.1016/j.marpetgeo.2023.106253
Received 4 January 2023; Received in revised form 30 March 2023; Accepted 2 April 2023
Available online 7 April 2023

hydrate is controlled by several factors, among which, temperature, pressure, ionic impurities in the water, and gas abundance and composition are key parameters.

Depending on the bottom water temperature and the availability of methane, methane hydrates typically occur under the ocean at water depths >400 m. In the Arctic Ocean, for example, methane hydrates occur in very shallow water depths at low temperatures. In marine sediments the increase in temperature with increasing sediment depth in

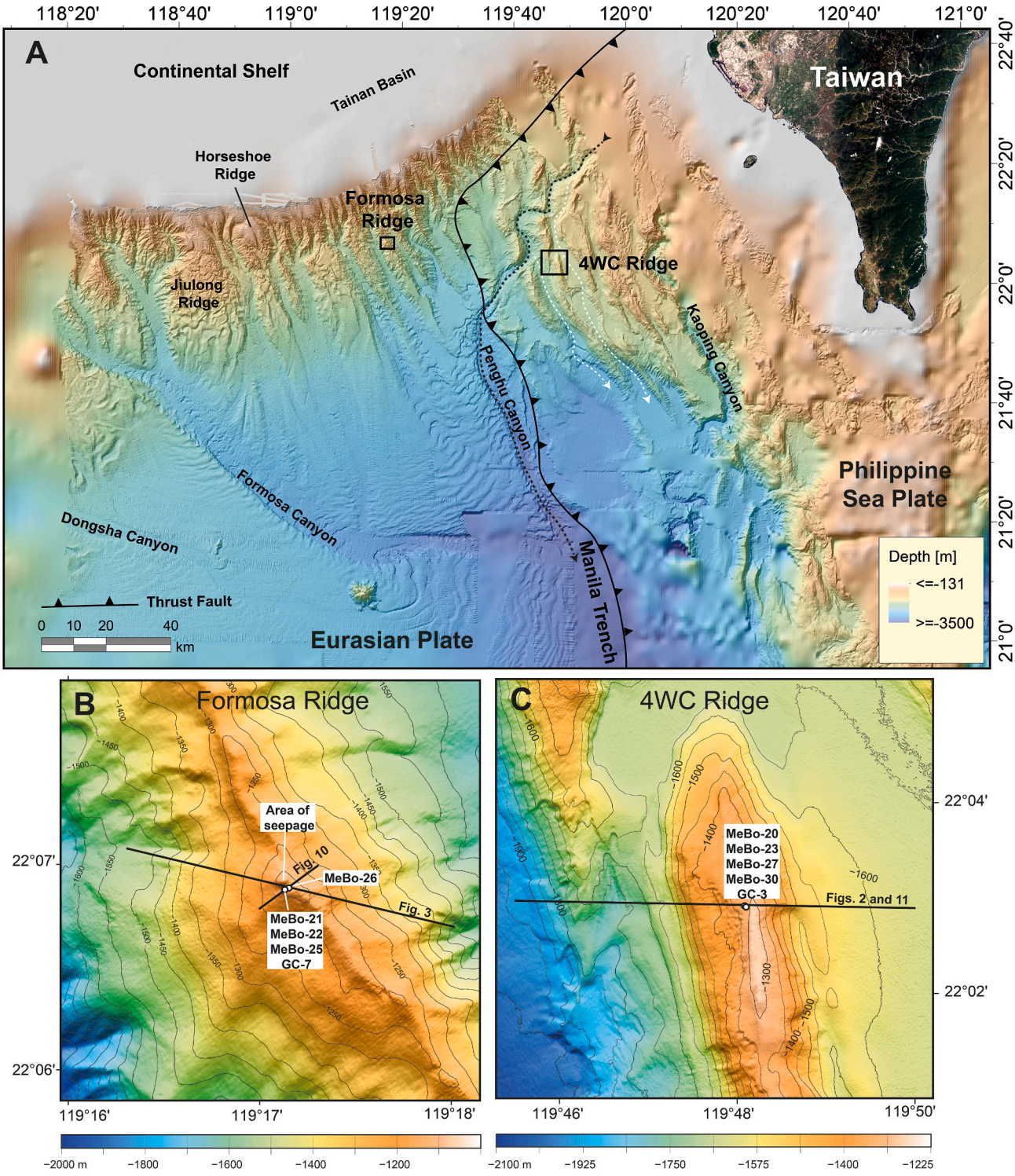

Fig. 1. Bathymetric map of southwest Taiwan showing the main seafloor morphological features and the location of Formosa Ridge at the passive continental margin and Four-Way Closure Ridge (4WC Ridge) at the active convergent margin (A). The outer deformation front of the accretionary wedge, which separates the Eurasian Plate in the west from the Philippine Sea Plate in the east, is also indicated [after Lin et al., 2008]. Present position of Penghu Canyon with black dotted line; former positions of Penghu Canyon west and east of 4WC Ridge are shown by white dotted lines. Bathymetric information are from multi-beam data of *R/V SONNE* cruises SO177 and SO266 and GEBCO data. The two black boxes give the positions of the two detail maps B and C. Detailed map from Formosa Ridge (B) showing the position of the seismic lines and the drilling location. High resolution map of 4WC Ridge (C) showing the location of the drill site close just west of the summit and the west/east running seismic profile.

accordance with the geothermal gradient defines a lower limit for methane hydrates, which varies depending on the depth of the seabed [Kvenvolden and Lorenson, 2001].

The presence of gas hydrate in sediments alters the physical properties by replacing parts of the water and gas in the pore space with a solid substance. Pore space and permeability are thereby reduced, which increases the acoustic impedance of hydrate bearing sediments. As a result, marine seismic reflection profiling is highly successful in detecting gas hydrates in marine sediments, because the lower boundary of hydrates is frequently shown by a bottom-simulating seismic reflection (BSR). Such BSRs mark the interface between relatively high acoustic impedance, hydrate-bearing sediment above and low acoustic impedance, free gas-bearing deposits, below [Shipley et al., 1979]. Beside seismic investigations, ocean drilling expeditions within the Deep Sea Drilling Project (DSDP), the Ocean Drilling Program (ODP), and the Integrated Ocean Drilling Program (IODP) have increased our knowledge on formation and distribution of marine gas hydrate deposits to a large extent [e.g., Kvenvolden, 1988; Paull et al., 2000a; Tréhu et al., 2003; Bohrmann and Torres, 2006; Riedel et al., 2006].

Since the eighties and nineties of the past century, the amount of field data led to the broad agreement that gas hydrates are a significant part of the natural environment with implications for society [Kvenvolden and Lorenson, 2001], and because of hydrate's global occurrences, natural methane hydrates received international attention. A global assessment suggested that methane hydrates might represent an important energy resource [Kvenvolden, 1998]. In addition, other important hydrate questions attracted attention, like the feedback between hydrate stability in the sediments and climate [Ruppel and Waite, 2020], the role of methane hydrate in the carbon cycle [Dickens, 2003], and the contribution of hydrate to seafloor stability of continental slopes and geohazards [Paull et al., 2000a].

The interest of Asian nations in using gas hydrate for energy production led to marine gas hydrate drilling programs that were conducted as part of national programs, like offshore Japan [Fujii et al., 2008], India [Collett et al., 2008], and South Korea [Kim et al., 2013]. In China, the northern continental slopes of the South China Sea moved into the focus of gas hydrate research, and gas hydrate deposits were investigated during several expeditions [e.g., Zhang et al., 2020]. The Shenu area, in particular, has been researched intensively over the past decade, and several production tests have been carried out [Li et al., 2018]. In the northeastern part of the South China Sea, offshore Taiwan, the tectonic regime changes from a passive continental margin in the northwest to an active margin characterized by compression and subduction in the East (Fig. 1) [Lin et al., 2008]. Gas hydrate presence and distribution was extensively investigated with geophysical methods [e.g., Berndt et al., 2019; Lin et al., 2009; Liu et al., 2006; Schnurle et al., 2004; Kunath et al., 2020, 2022] and geochemical studies [e.g., Chen et al., 2017; Chuang et al., 2013].

In 2018 very shallow (5.5 mbsf) gas hydrate samples were recovered in the core catcher of two piston cores from Good-Weather Ridge and South Yuan-An East Ridge, both located at the active continental margin [Huang et al., 2021]. Drilling of gas hydrate deposits was lacking until 2018, when a Taiwanese/German expedition used *R/V SONNE* (cruise SO266) and the mobile drilling system MARUM-MeBo200 to drill sediment cores. During the cruise, indications for gas hydrate deposits were found by drilling in both regions at the passive and active continental margins of the northern South China Sea. Here, we present new drilling-derived data related to methane hydrate occurrence from two drill sites, Formosa Ridge and Four-Way Closure Ridge (Fig. 1) to illustrate the fundamental difference in gas hydrate dynamics between a passive and an active margin.

2. Geological setting

The northeastern area of the South China Sea (Fig. 1) is part of the Taiwan collision zone, where the passive continental margin of China, represented by a Cenozoic sediment sequence of the Tainan basin, collides with the northern Luzon island arc [Bowin et al., 1978]. South of the passive margin, approximately south of 22°N, the lithosphere of the Eurasian Plate is subducting to the East beneath the Philippine Sea Plate along the Manila Trench (Fig. 1 [Lin et al., 2009]).

Convergence rates are high and were deduced to be between 7–9 cm/year [Seno et al., 1993]. North of 22°N latitude, the collision formed a broad accretionary wedge including a series of accretionary ridges that gradually change orientation from NE-SW in the North to NW-SE in the South (Fig. 1). The slope basins between the accretionary ridges are often affected by sediment gravity flows that get deflected from their regional down slope direction by ponding against the accretionary ridges. Some large canyons, which cut through the shelf from the mouths of the Taiwanese rivers, alternate their direction due to the rugged slope morphology (Fig. 1). This results in the formation of canyon segments with relatively steep slopes, nearly perpendicular to the ridges, and sections with slightly flatter slopes parallel to the elongated accretionary ridges [Hsiung et al., 2014].

In this way, the slope morphology caused by the accretionary wedge has a considerable influence on the downslope transport of sediment suspension flows, which might be very frequent due to the seasonal monsoons. The accretionary wedge has been divided into a backthrust domain, an upper slope domain, and a lower slope domain [Reed et al., 1992]. The lower slope domain was subdivided into a rear segment and a frontal segment based on the tectonic settings [Lin et al., 2009]. The upper slope domain reveals extensive mud diapirism, mud volcanism, and associated seafloor seepage [Chen et al., 2014; Chiu et al., 2006], whereas the lower slope domain is an area of active thrusting, folding and gas seepage as well [Klaucke et al., 2016; Lin et al., 2009; Liu et al., 2006(Tseng et al., 2023)].

The southern part of Four-Way Closure Ridge represents a typical asymmetric anticline structure above a west-verging blind thrust [Klaucke et al., 2016]. The ridge is about 10 km long and 2–3 km wide and rises up to 350 m above the surrounding seafloor (Fig. 1). The crest of the ridge is oriented NNW-SSW and culminates in around 1280 m water depth. Klaucke et al., [2016] and (Tseng et al., 2023) described the details in bathymetry and backscatter pattern of the ridge and the surrounding area. Slump scars of different scales are widely distributed along both flanks of Four-Way Closure Ridge with a large scar of 4 km lengths developed along its eastern flank [Klaucke et al., 2016]. A 3-D seismic data set across the ridge imaged a more complex accretionary structure than just a simple anticline [Kunath et al., 2020]. The Four-Way Closure Ridge is the larger anticline of a double anticline structure (Fig. 2). The west-east seismic profile shows an additional accretionary ridge west of Four-Way Closure Ridge which was named Ridge A by Kunath et al. (2020). To the east, the western part of the adjacent slope basin is well imaged (Fig. 2). The uppermost sediments beneath the crest show the dipping strata by stratified parallel reflections of the eastern flank with onlap structures of the youngest sediments. The western flank is less well imaged and seems to be of complex origin including an additional fold structure with thrust faults (Fig. 2). The BSR subbottom depth is 450 ± 25 mbsf underneath the ridge and gets shallower underneath the slope basin (Kunath et al., 2020).

The passive continental margin west of the deformation front is characterized by a series of ENE-trending normal faults on the shelf and at the margin [Lin et al., 2009]. The seafloor morphology of the slope shows deeply incised, NW-SE trending canyons perpendicular to the strike of the slope (Fig. 1). Steep flanks of the canyons start close to shelf break in 200 m water depth. The canyons are well developed down to approximately 2000 m water depth . Formosa Ridge (Fig. 1) is one of the ridges on the passive continental margin that is formed by canyon incision into the sediment of the slope. Bathymetric mapping imaged Formosa Ridge as an elongated 45 km-long ridge that extends from the mid-slope of the continental margin in southeastward direction to the South China Sea abyssal plain near the Manila Trench [Hsu et al., 2018].

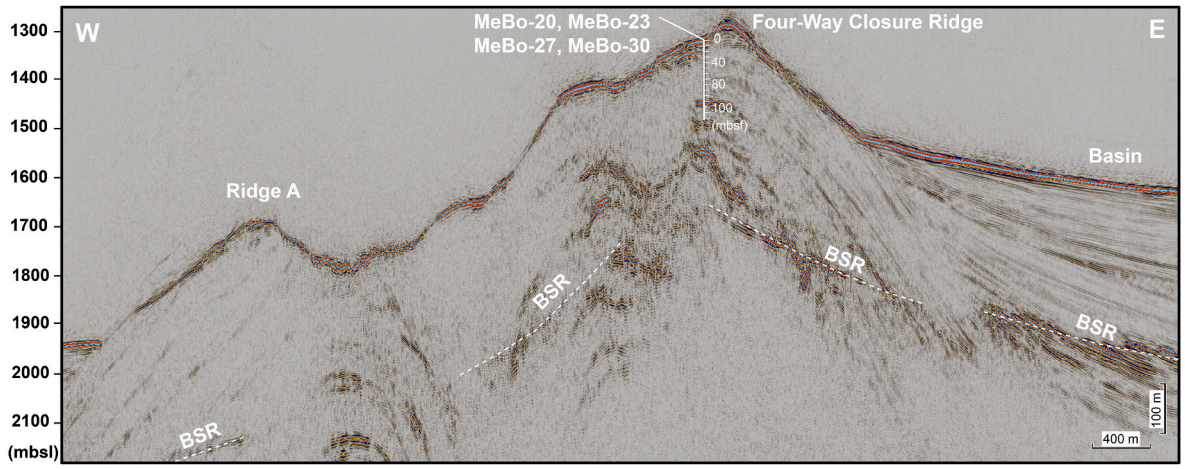

Fig. 2. West-East running seismic profile crossing Four-Way Closure Ridge, an asymmetric accretionary ridge of the active margin, with interpreted bottom simulating seismic reflector (BSR) after Kunath et al. (2020). Positions and drilling depths of MeBo drillings are also indicated. The location of the seismic profile is shown in Fig. 1C.

Two summits exist along its crest, with the northern peak situated at 1088 m water depth and the southern peak positioned at 1125 m water depth.

A site of active strong gas seepage known from the southern summit of Formosa Ridge [Liu et al., 2008] became a hot spot for biogeochemical studies [Feng et al., 2018]. Seismic data show that undulating sedimentary features of the lower slope represent sediment waves and that truncations of reflectors are caused by formerly incised and now refilled canyons [Berndt et al., 2019]. Sediments underneath the crest of the ridge are horizontally stratified (Fig. 3) except the youngest, uppermost deposits, which overlie a well-defined unconformity. Below the southern peak, a vertical seismically blank zone rises from the depth of the BSR and up to the crest, where a seep site is located at the seafloor [Berndt et al., 2019]. The vertical structure (Fig. 3) in the seismic data was interpreted as a fluid conduit representing gas charged deposits extending from below the BSR in subbottom depth of more than 400 mbsf. The high-resolution 3D seismic data were used to analyze the seismic character of the conduit in detail and an episodic activity of gas transport within the conduit to the seafloor was postulated by Kunath et al. (2022).

3. Data and methods

During R/V SONNE cruise SO266 in 2018, sediment samples were obtained from Formosa Ridge and Four-Way Closure Ridge by gravity- and MeBo coring (Tables 1 and 2) [Bohrmann et al., 2019]. For deeper

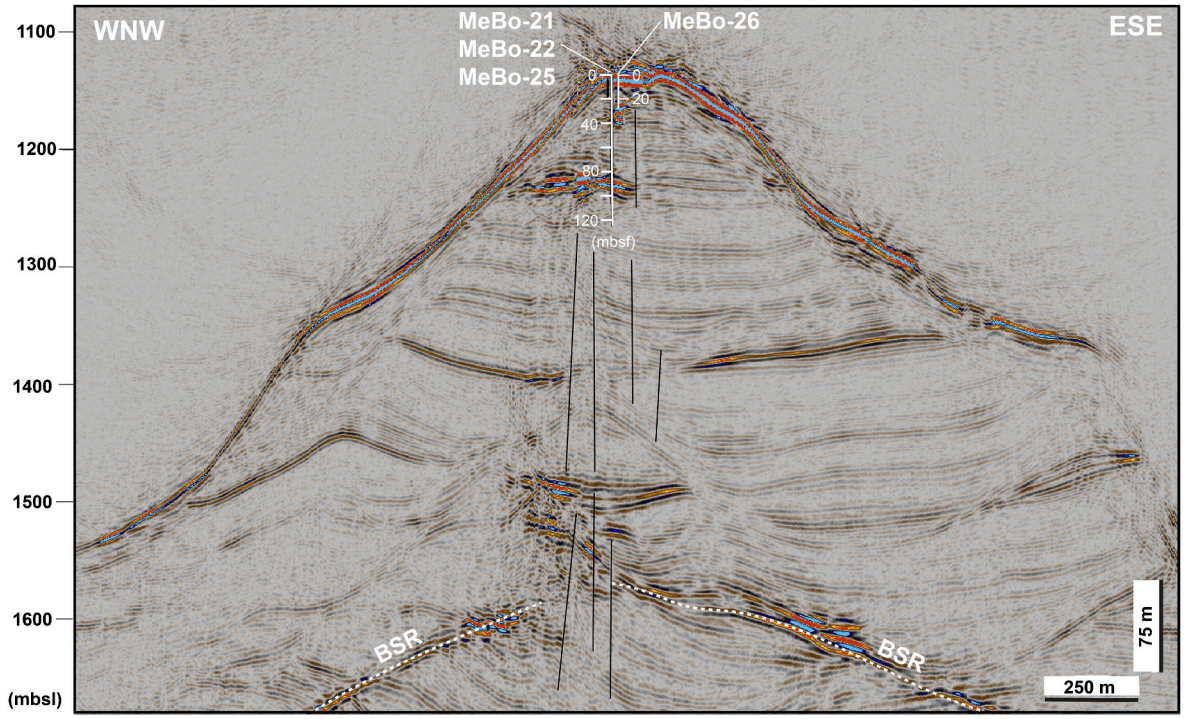

Fig. 3. The WNW-ESE striking seismic profile over Formosa Ridge from the passive margin is showing a complex sediment sequence down the BSR. The disrupted BSR in the center and highly variable amplitudes above were interpreted as a conduit structure which allows for gas ascent from below the BSR to the seabed and causes excape of methane bubbles into the water column (Berndt et al., 2019). Suspected near-vertical faults are indicated by black lines. Positions and drilling depths of MeBo drilling are also shown. For location of the profile and the drill site see Fig. 1B.

Table 1
Locations of gravity cores (GC) and MeBo drilling cores (MeBo) during cruise SO266; FWCR = Four-Way Closure Ridge, SSFR = Southern Summit Formosa Ridge. GeoB numbers are internal numbers of the MARUM GeoB Core Repository at the University of Bremen.

Station Number	GeoB Number	Location	Latitude N	Longitude E	Water Depth [m]
GC-3	23205–1	FWCR	22°02.891′	119°48.098′	1322
MeBo-20	23204–1	FWCR	22°02.916′	119°48.091′	1322
MeBo-23	23216–1	FWCR	22°02.919′	119°48.089′	1322
MeBo-27	23231–1	FWCR	22°02.919′	119°48.083′	1342
MeBo-30	23240–1	FWCR	22°02.926′	119°48.075′	1324
GC-7	23226–1	SSFR west	22°06.887′	119°17.134′	1142
MeBo-21	23212–1	SSFR west	22°06.888′	119°17.130′	1142
MeBo-22	23213–1	SSFR west	22°06.886′	119°17.136′	1142
MeBo-25	23227–1	SSFR west	22°06.886′	119°17.137′	1142
MeBo-26	23230–1	SSFR east	22°06.887′	119°17.147′	1141

drilling, we used the seafloor drill rig MARUM-MeBo200 (https://www.marum.de/en/Infrastructure/Sea-floor-drill-rig-MARUM-MeBo200.html), a robotic drill that is deployed on the seafloor and remotely controlled from the vessel in order to sample the seabed by rotary core drilling. MeBo200 is a further development of MeBo70 which is also managed and deployed by MARUM at the University of Bremen [Freudenthal and Wefer, 2013]. MeBo cores were mostly taken from the seafloor by pushing a core barrel downwards into soft sediments. When sediments became more indurate we changed to a rotary drilling method. Sediment cores from push coring have diameters of 55 mm whereas rotary cores are 61 mm in diameter. A water pump provides sea water for flushing the drill string, for cooling of the drill bit and for removing the drill cuttings.

On Four-Way Closure Ridge we recovered sediment cores from three holes, MeBo-20, -23, and -30 (Table 2) at 1322, 1324, and 1342 m water depths, respectively [Bohrmann et al., 2019]. In these we sampled sediments by drilling to a maximum depth of 124.53 mbsf (Table 2). Sediment recovery rate was between 74.5 and 92.3% (Table 2). A fourth hole, MeBo-27, was drilled to 140.4 mbsf without coring and a Spectrum Gamma Ray (SGR) log was measured to the surface (Table 2). On Formosa Ridge we drilled four holes (MeBo-21, -22, -25, and -26) in water depths of 1141 and 1142 m and reached a maximum depth of 126.40 mbsf in Hole MeBo-25 (Table 2). Sediment recoveries ranged between 63.2 and 91.5% (Table 2).

The borehole logging tools that were used with the MeBo200 drilling system are autonomous slim hole tools. They are equipped with a memory logger containing batteries and data loggers for measuring the physical formation properties in the borehole autonomously. When the maximum coring depth was reached the inner core barrel was replaced by the respective logging tools. The tools are placed below the drill bit and are pulled up the borehole together with the drill pipe during recovery of the drill string (logging while tripping; Freudenthal and Wefer, 2013; Kück et al., 2021). We used a Spectrum Gamma Ray (SGR) probe in combination with either a Dual Induction (DI) tool (MeBo-25) or a Memory Acoustic Tool (MAT; MeBo-22 and -27). Data of the MAT will be analyzed in another study. The SGR consists of a 250 mm-long caesium iodide crystal, 38 mm in diameter, connected to a photo-multiplier. Light impulses that are generated by gamma ray collision with the scintillation crystal are counted and analyzed across the energy spectrum. Sediment resistivity was calculated from electrical conductivity which was measured with the DI tool. The tool provides two measurements, and for this work we only used the medium induction sensor with a 100 kHz drive signal and a depth range of 0.65 m (horizontal into the formation). The resistivity range is 0.5–100 Ωm, the vertical resolution is about 0.8 m [Bohrmann et al., 2019].

Since the uppermost sediments in MeBo boreholes are very often disturbed during landing of the MeBo and initial construction of the drill string, we also collected gravity cores (max. 10 m) at each site to sample the topmost seabed with better quality (Table 1). Sampling of the gravity and MeBo cores followed the standard procedure of the MARUM GeoB Core Repository. This means, MeBo cores are 3.5 m-long sections and after the plastic core liners are retrieved from the core barrel, temperature was continuously measured by scanning the core liners with an infrared (IR) camera for detecting potential gas hydrate dissociation in the liner. For the IR data, a ThermaCam SC 640 from FLIR Systems was used. It measures temperature in a range from −40 °C to 120 °C with a precision of 0.1 °C and an accuracy of ±2 °C. During the measurements the camera was fixed on a tripod. IR images were taken with a focal distance of 150 cm between lens and surface of the liner. Each image covered approximately 60 cm of core length. Images were taken every 50 cm to guarantee an overlap for the following stitching process using an external scale with temperature tick marks. This method was developed in the frame of ODP to obtain a continuous record of a proxy for the spatial distribution of gas hydrates, and has been used in many drilling campaigns [e.g., Tréhu et al., 2003; Weinberger et al., 2005].

After lengthwise splitting of the cores into archive and working halves, the working halves were sampled for pore water, physical properties and sedimentology. Archive halves were digitally imaged with a Line Scanner, and used for sediment analysis and core description [Bohrmann et al., 2019]. For pore water analysis, 5 cm-thick slices were taken in approximately 20–40 cm intervals from the gravity cores (GC). Slices of 25 cm were taken from the MeBo cores from homogenous fine-grained sediments at intervals of approx. 1 m. In the case of lithological changes, the sampling distances were significantly shorter and smaller sample slices were taken with a thickness of 3–4 cm. Sampling of the core rim was avoided in order to minimize sampling of pore water

Table 2
List of MeBo drilling location, depth, core length, recovery and tools taken during cruise SO266 (SGR = Spectrum Gamma Ray probe; DI = Dual Induction tool; MAT = Memory Acoustic Tool).

Station no. GeoB no.	Area	Drilling depth [m]	Coring length [m]	Recovery [m]	Recovery (%)	Logging tools
MeBo-20 GeoB23204-1	FWCR	21.40	14.00	13.01	92.9	–
MeBo-23 GeoB23216-1	FWCR	126.35	104.85	88.43	85.5	–
MeBo-27 GeoB23231-1	FWCR	143.90	No coring	–	–	SGR, MAT
MeBo-30 GeoB23240-1	FWCR	126.35	10.45	7.78	74.5	–
MeBo-21 GeoB23212-1	SSFR west	14.40	14.40	5.97	85.3	–
MeBo-22 GeoB23213–1	SSFR west	108.98	99.01	90.60	91.5	SGR, MAT
MeBo-25 GeoB23227-1	SSFR west	126.40	21.90	14.59	66.6	SGR, DI
MeBo-26 GeoB23237-1	SSFR east	23.93	20.08	12.68	63.2	–

that has potentially been contaminated with bottom water that was filling the space between the liner and the core.

Subsequently, the pore water was extracted in the ship's cold room (4 °C) using centrifugation for GC samples and a low pressure-squeezer (argon at 3–5 bar, occasionally up to 7 bar) for MeBo200 samples. While squeezing, the pore water was filtered through 0.2 μm cellulose acetate Whatman filters and collected in recipient vessels. Aliquots of the extracted pore water were subsampled for various onboard and further shore-based analyses. Pore water chloride concentrations were determined onboard by ion chromatography [Bohrmann et al., 2019], which was also used as a proxy for the presence of gas hydrate [Tréhu et al., 2004]. Sediment samples for bulk carbonate measurements were taken in approx. 2 m intervals. Particulate organic carbon and calcium carbonate were measured onshore by combustion with a Vario EL III elemental analyzer in the CN mode. Total carbonate was determined by subtracting organic carbon (pre-treatment with 2 N HCl) from total carbon.

4. Results

4.1. Lithologies and physical properties of drilled deposits

The seafloor sediments drilled at Formosa Ridge and Four-Way Closure Ridge consist predominantly of fine-grained terrigenous-dominated deposits. Drilling provided, however, a wealth of information on changes in the depositional environment, and how the sediments were overprinted by fluid migration and post-depositional gas hydrate formation and dissociation.

4.1.1. Drilling at southern summit of Formosa Ridge

At Formosa Ridge (Figure 1 and 3) we sampled the subsurface at Holes MeBo-21, -22, and −25 along with Gravity Core GC-7. The drilled holes are less than 30 m away from each other. Further information is available from well-log data measured in Hole MeBo-22. By combining those data, a more or less continuous sediment sequence to 126.40 mbsf (Fig. 4) was achieved. The deepest borehole is MeBo-25. It reached a drilling depth of 126.40 mbsf and both resistivity and spectrum gamma radiation were logged at this site (Figs. 4 and 7; Table 2). The lithology of the cored sediments is dominated by homogeneous dark gray clay with scattered occurrences of foraminifers, small shells of gastropods visually detected on the surface of the core. Several intervals show spotted black aggregates of iron sulfides. An ash layer was found at a depth interval of 72.04–72.10 mbsf. In Hole MeBo-22, there are light gray and dry patches of a few centimeters in diameter from 84.40 mbsf (Core 23P) to 97.27 mbsf (Core 27P).

Authigenic carbonate precipitation represented by higher carbonate values and nodules are present from 87.22 mbsf to 93.80 mbsf (Fig. 4). They correlate with increased gamma ray values including a distinct

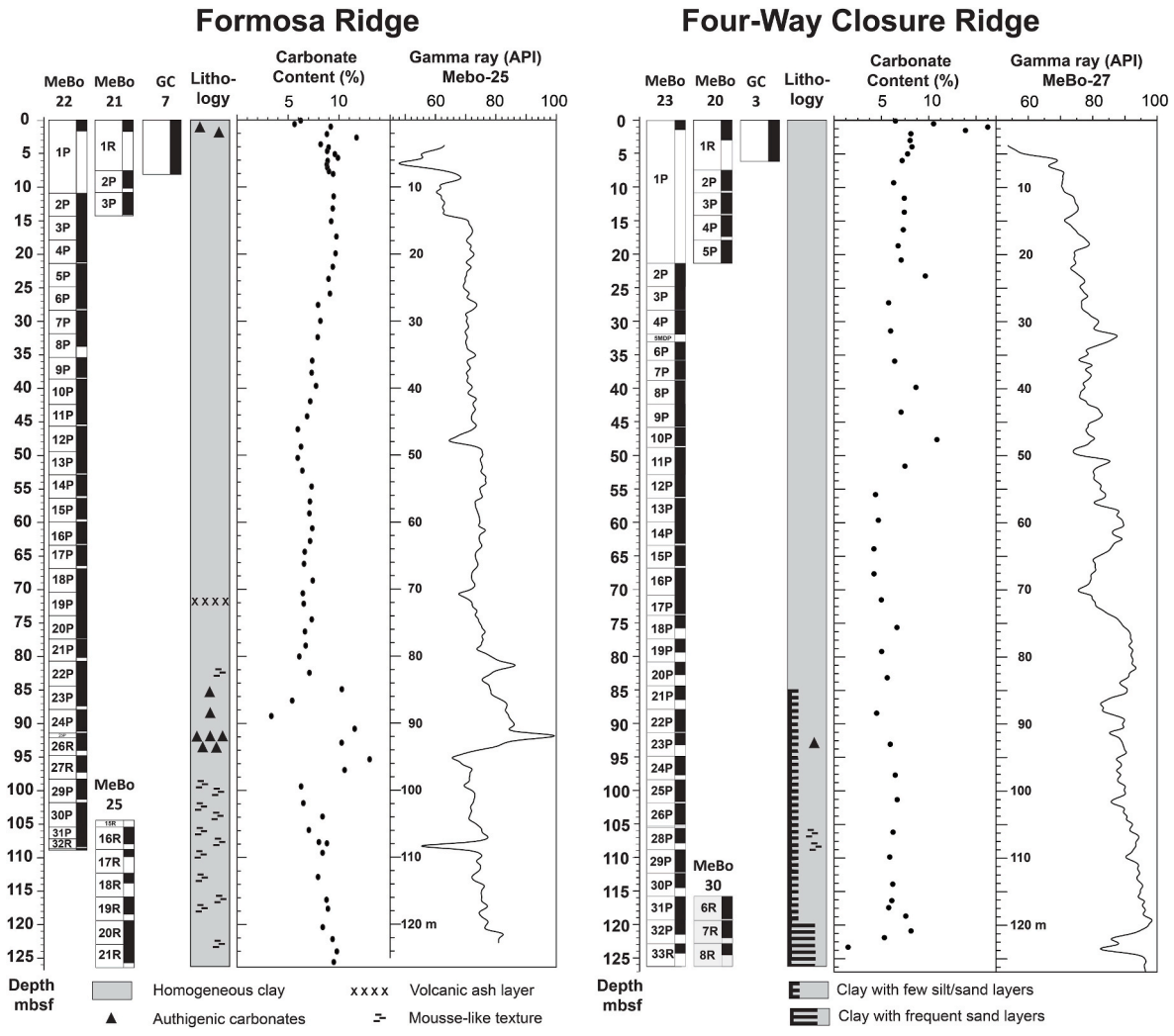

Fig. 4. Lithological sequences from both areas drilled, Formosa Ridge and Four-Way Closure Ridge. From left to right for each area: Downhole succession of cores and recoveries (P = push core, R = rotary core) are shown by a black box in each core. The lithological column with specific details of the sediments is followed by carbonate contents and gamma ray data.

high peak at 92 mbsf. In general, carbonate contents of the sediment vary between 5 and 10%. They decrease downwards to near 5% and increase with depth in the lowermost 25 m of drilled sediments (Fig. 4). Within the interval with carbonate nodules the carbonate contents scatter, but are mainly higher than 10%. This increase together with the carbonate nodules suggests authigenic carbonate formation in this interval.

Carbonate precipitation seems widespread in Hole MeBo-22 cores 23P–27R (Fig. 5) and correlates with a change from push coring in MeBo-25 to rotary drilling in MeBo-26. For both MeBo-22 and MeBo-25 at Formosa Ridge, scattered mousse-like sediment textures (Fig. 4) occur from 98.30 mbsf at MeBo-22 to 124 mbsf at MeBo-25. Some of the sediment intervals with mousse-like textures at both MeBo-22 and MeBo-25 Holes were also associated with soupy sediments. An ash layer found by visual inspection at Core 19P 25–35 cm (72.10 mbsf) was also associated with high magnetic susceptibility.

4.1.2. Drilling at Four-Way Closure Ridge

At Four-Way Closure Ridge (Figs. 1 and 2) MeBo200 was deployed four times (MeBo-20, -23, -27 and -30) in water depths ranging from 1322 m to 1342 m. The drilled and cored holes are less than 70 m away from each other. Together with Gravity Core GC-3, all sediment information was combined with the gamma ray log and carbonate contents (Fig. 4). Sediment cores at Holes MeBo-23 and MeBo-30 were collected down to 124.38 mbsf and 124.53 mbsf, respectively. The lithology of the cored sediments is dominated by homogeneous dark gray clay with scattered presence of foraminifera, small shells of bivalves or gastropods. A few intervals show spotted black aggregates of iron sulfides. Silt/sand patches and thin sorted silt and sand layers start to appear from 85 to 120 mbsf, while distinct sand layers become more frequent and thicker downward from around 120 to 125 mbsf. These are up to 30 cm-thick for individual sand horizons (Figs. 4 and 6) which often showed a fining upwards trend.

With the exception of the uppermost sediments in Gravity Core GC-3, carbonate contents are less than 10% and very often around 5% (Fig. 4). Spectrum gamma radiation increases with depth. However, the data show variability. Distinctly lower values such as those between 65 and 72 mbsf, cannot be attributed to observed lithological changes in the cores. An exception is the lowermost interval between 120 and 125 mbsf, where distinctly lower gamma ray values clearly correlate with the presence of thick sand layers (Fig. 4). There are a few soupy layers and intervals with mousse-like sediment textures, especially in MeBo-23 Core 28P (Fig. 6).

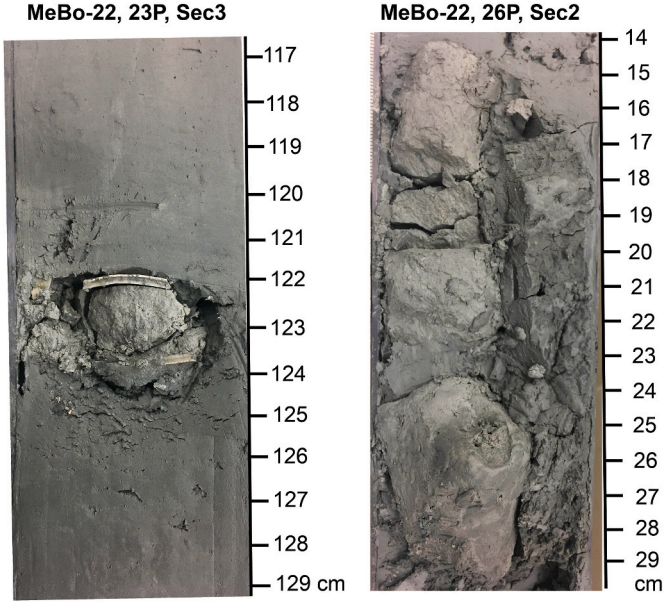

Fig. 5. Close-ups of sediment features in MeBo Hole-22 drilled at southern summit of Formosa Ridge. Cm-sized carbonate concretion bordered by molluscan shells (left). Elongated vertical authigenic carbonate nodules in sediments of higher carbonate content (right).

4.2. Pore water chloride concentrations and gas hydrates

Apart from other geochemical parameters, chloride concentrations of the pore water from the cored sediments were measured in order to document the occurrence of gas hydrates and the gas hydrate saturation in the available pore space. During core recovery, dissociation of hydrate releases fresh water into the ambient pore water and leads to a reduction of the pore water chlorinity by dilution, as has been reported for many gas hydrate-bearing marine sediment sequences [Kim et al., 2013; Paull et al., 2000b; Tréhu et al., 2006; Ussler, 2001; Hong et al., 2021].

Chloride concentrations less than background values in most cases represent past gas hydrate that has dissociated during core recovery. Defining the background profile in chlorinity of a sediment core is critical, because other diagenetic processes may have influenced the pore water chloride concentration profile as well. Specifically, dehydration of hydrous minerals, as it occurs during smectite to illite transformation, can cause freshening and low Cl^- fluids which have been observed in many continental margins [Kastner et al., 1991; Torres et al., 2004]. Since release of freshwater from diagenetic mineral reactions affects longer depth intervals and does not cause abrupt changes in pore water profiles between low and high Cl^- concentrations, it is assumed that the background curves of Cl^- at both sites are not or very slightly influenced by fresh water released from diagenetic mineral reactions.

At Formosa Ridge, dissolved chloride has a typical background concentration of around 560 mM. There are two well-defined intervals at 13–39 mbsf and at 98–120 mbsf (Fig. 7) with anomalously low chloride concentrations. The upper interval with its lowest Cl^- concentration of 511 mM occurs in Cores 2P 9P of MeBo-22 and in Core 3P of MeBo-21 (Fig. 7). The deeper interval that is characterized by negative chloride concentration anomalies is between 98 and 120 mbsf corresponding to Cores 29P 32R of MeBo-22 and Cores 16R–20R of MeBo-25 (Fig. 7). Here, Cl^- concentrations range between 430 and 500 mM with a minimum of 388 mM in Core 18R of MeBo-25.

At Formosa Ridge, a linear background curve was considered with Cl^- concentrations ranging from 560 mM at the top of the sediments to 570 mM at the bottom of the boreholes. Based on measured Cl^- concentrations and estimated background concentrations, we calculated the gas hydrate saturation of the pore space using equations given by Ussler, 2001. Hydrate saturation calculated this way is shown in Fig. 7. Calculated hydrate saturation below 1% is not shown in the diagram, because of the resolution of the data. In general, the calculated hydrate saturation in the upper interval (13–39 mbsf) ranges between 1% and 10% and is significantly higher with saturations between 10 and nearly 40% in the lower interval (98–120 mbsf) (Fig. 7).

In the sediments drilled at Hole MeBo-23 at Four-Way Closure Ridge, pore water Cl^- concentrations deviating from background values start at depth of Core 15P in 65 mbsf and occur downward with varying concentrations (Fig. 8). The chloride background concentration was assumed as a linear trend between 550 mM at the seafloor and 570 mM at the bottom of the cored sediment sequence in 124 mbsf. Negative chloride concentration anomalies between 65 and 120 mbsf vary between 500 mM and the background concentration with few exceptions in Core 28P of MeBo-23, where the lowest Cl^- concentration of 429 mM was also measured (Fig. 8).

The highest fluctuation in Cl^- concentrations was measured in Cores 32P and 33R of MeBo-23 and Cores 7R and 8R in MeBo-30. According to these negative chloride concentration anomalies, gas hydrate saturation below 65 mbsf is mostly less than 20% of the pore space, and often less

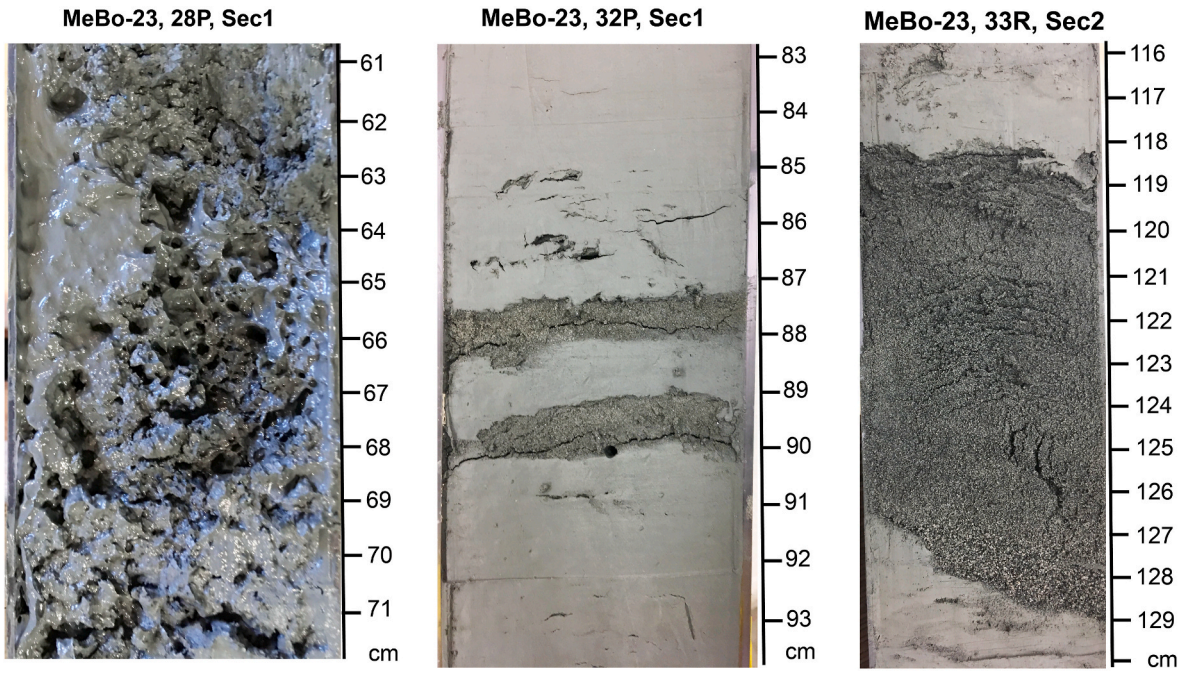

Fig. 6. Photographs of core MeBo-23 from Four-Way Closure Ridge. Mousse-like, partly soupy sediment texture in the core are representing decomposed hydrate (left), two thin fine-grained sand turbidites in otherwise homogenous silty clay (middle), sand turbidite showing fining upwards sequence (right).

than 10% of the pore space. However, there are two exceptions: Gas hydrate saturation in a few samples in Core 28R reached 23% and 29%, and the chloride data suggest a distinct peak in gas saturation of up to nearly 80% of the pore space for the deepest sediments below 120 mbsf (Fig. 8).

In Core 7R of MeBo-30 we took pore water samples in closer spacing because many sand layers are intercalated (Fig. 9). Temperature anomalies were measured with the IR camera over the entire core and documented gas hydrate-bearing layers by cold spots. This is well shown by the IR images and quantitatively by the plot of the ΔT values (Fig. 9). Cold spots are well documented from other hydrate provinces where they are caused by endothermic hydrate dissociation when sediment cores leave the gas hydrate stability zone [Tréhu et al., 2003; Tréhu et al., 2004]. A total of six horizons with clear temperature anomalies were detected during the IR temperature measurements. All of these coincide with sand layers. The pore water samples in Core 7R were taken from different lithologies. Four of the pore water analyzes, which sampled sand layers show clear negative chloride anomalies, while the six analyzes of the intercalated clay layers show the background chloride concentrations or slightly positive anomalies (Fig. 9).

5. Discussion and interpretation

Seismic investigations revealed that a gas hydrate-related bottom simulating seismic reflector is present throughout vast areas southwest of Taiwan [Chi et al., 1998; Liu et al., 2006; Schnürle et al., 2011]. This observation is unequivocal evidence that gas hydrates exist both in the passive continental margin of the South China Sea and in the active accretionary wedge. Geochemical investigations on methane production, migration and seepage in the area southwest of Taiwan indicate that seafloor seepage exists both in the active margin and in the passive margin, but is more frequent in the active margin [Chen et al., 2017; Chuang et al., 2010]. Composition of light hydrocarbons and isotope analyses revealed a predominance of microbial methane in the sediments of the passive margin, whereas thermogenic methane was partly more found in deposits of the active margin especially at the upper slope and onshore mud volcanoes [Chen et al., 2017]. Up to *R/V SONNE* cruise SO266 in 2018 no boreholes were drilled in this hydrate province, and thus the new drilling results provide unprecedented constraints on hydrate presence and distribution within the uppermost 126 mbsf of the gas hydrate stability zone.

MeBo drillings in both areas on Formosa Ridge and Four-Way Closure Ridge were unable to recover methane hydrates as solid matter. Nevertheless, several methane hydrate proxies, such as geochemical, physical and lithological indicators, and sediment texture confirm the presence of methane hydrates in various intervals of the sediment formations. While massive methane hydrate layers have been drilled and recovered successfully with MeBo in several other geological settings [Himmler et al., 2019; Pape et al., 2020a, b], the absence of intact hydrates in the core material obtained during SO266 suggests that massive gas hydrate were not penetrated.

Instead, it is inferred that the methane hydrates drilled here, primarily forms fine crystals disseminated in the sediment or that they exist in very thin veins, allowing them to decompose during the long process of retrieving the MeBo drill rig through the water column, and the recovery of the core barrels on deck until opening the sediment-filled liners. The process of MeBo recovery until the time the core liner are accessible takes much longer time than gravity coring, and typically results in a greater portion of dissociated hydrates. Dissociation presumably begins immediately when the hydrate leaves the gas hydrate stability zone, which is controlled by the pressure and temperature structure in the water column. Given the oceanographic regime off Taiwan this corresponds to approximately 630 m depth below the sea surface.

The dissociation of small hydrate particles is relatively fast due to their large surface area to volume ratio, while massive methane hydrate layers have a lower surface area to volume ratio, and a self-preservation effect is retaining the hydrate [Sloan and Koh, 2008]. This self-preservation effect of hydrate is thought to be linked to the endothermic nature of hydrate dissociation, which can form a layer of water ice on the hydrate surface. Such an ice coating may seal the interior hydrate, thus preventing it from further dissociation [Takeya et al., 2005].

Therefore, we suggest that most of the cores sampled contained only disseminated pore filling methane hydrate that decomposed and released fresh water and methane during the recovery of the cores. This

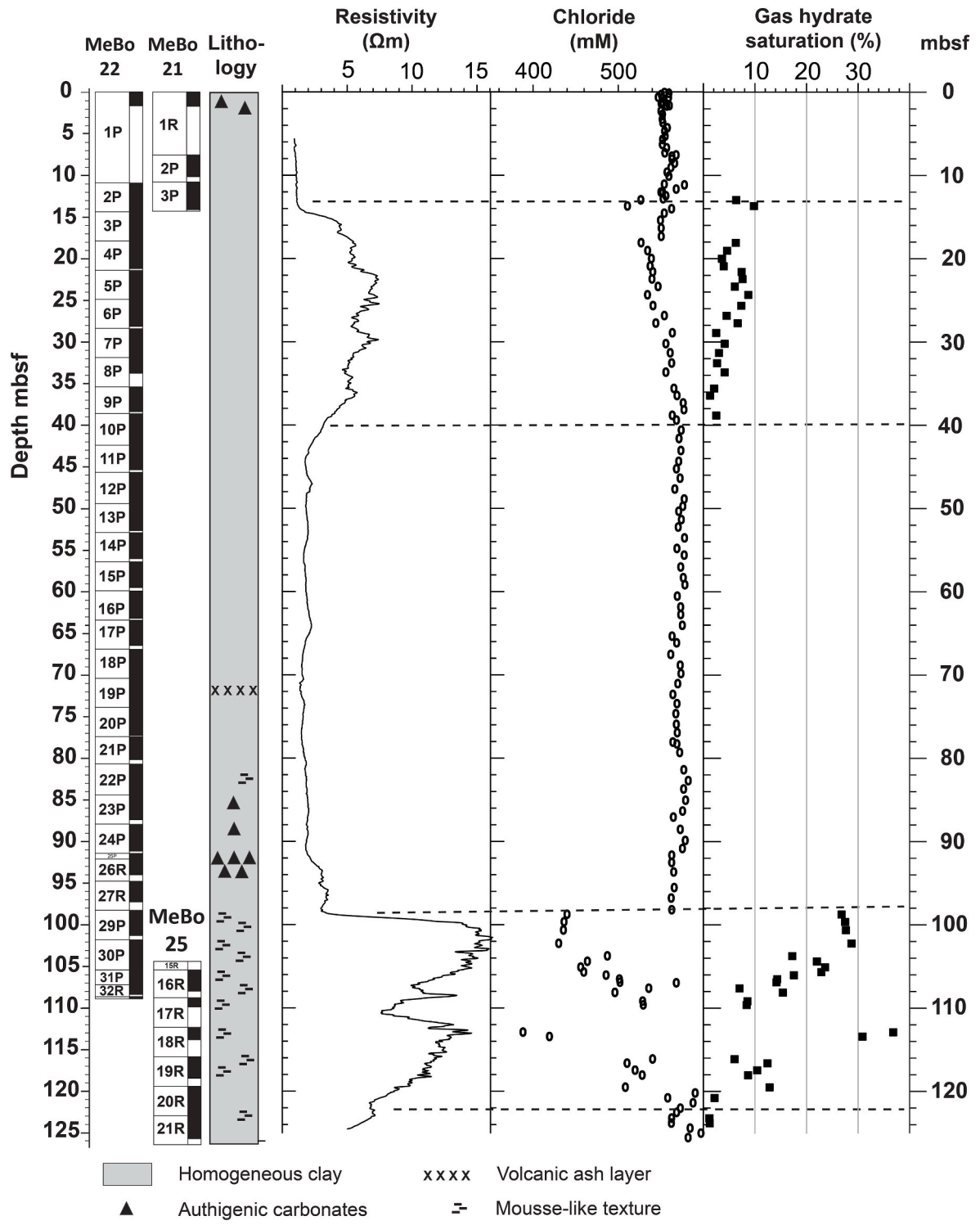

Fig. 7. Results of MeBo cores from the southern summit of Formosa Ridge. From left to right: Cores labeled (P = push core, R = rotary core) and sediment recoveries (shown by a black box in each core) related to depth, summary of lithological findings in the cores, resistivity data from borehole logging of Hole MeBo-25, pore water chloride concentrations and related gas hydrate saturation estimations derived from chlorinity.

would explain the soupy texture in sediment core intervals with pore water chloride anomalies (Figs. 6 and 8). This is also corroborated by IR temperature anomalies and resistivity data from borehole logging which were measured in-situ, when hydrates still existed in the deposits. From all measured gas samples of the MeBo cores, methane is the dominant gas phase with more than 99.8 mol-% of light hydrocarbons (T. Pape personal communication) and we, therefore expect that hydrate structure I was the prevailing structure of the hydrates (Sloan and Koh, 2008).

5.1. Gas hydrates at Formosa Ridge

The geochemical, sedimentological, and borehole logging data suggest that gas hydrates were present in the sediments of the three holes,

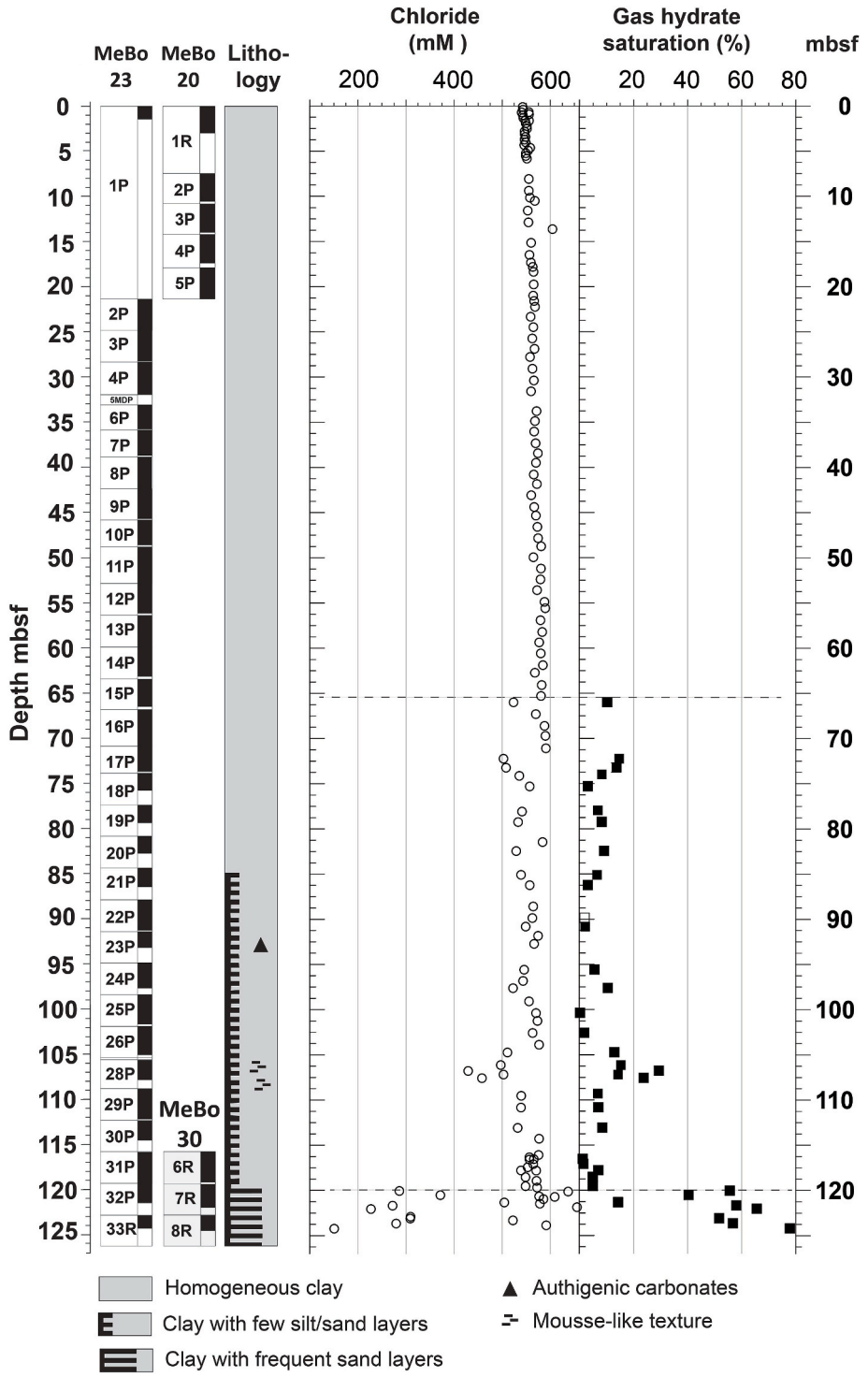

Fig. 8. Results of MeBo cores from the Four-Way Closure Ridge. From left to right: Core recoveries related to depth, summary of lithological findings in the cores, pore water chloride concentrations and some related gas hydrate saturation estimations derived from chlorinity.

MeBo-21, -22 and -25 at Formosa Ridge at different depth intervals (Fig. 7). The pore water sulfate concentration profiles indicate the sulfate-methane interface (SMI) is near 10 mbsf [Bohrmann et al., 2019], which means that no methane hydrates are stable within the uppermost 10 m of the sediments due to methane consumption by the anaerobic oxidation of methane [Boetius et al., 2000]. Gas hydrates will not exist well below the SMI since methane concentration needs to increase downwards first until it reaches solubility.

First indications for the presence of methane hydrates are slightly lower pore water chloride concentrations compared to background concentrations from about 13 mbsf downwards. This upper interval showing hydrate saturations between 1 and 10% of pore space extends to a depth of 39 mbsf (Fig. 7). Between 39 and 98 mbsf, pore water chloride concentrations deviate only insignificantly from the background concentrations, indicating the absence of detectable gas hydrates in this depth range. Below 98 mbsf to around 120 mbsf, fluctuations in the chloride concentrations show variable gas hydrate saturations, but with a range of 10–40% the saturation values are significantly higher

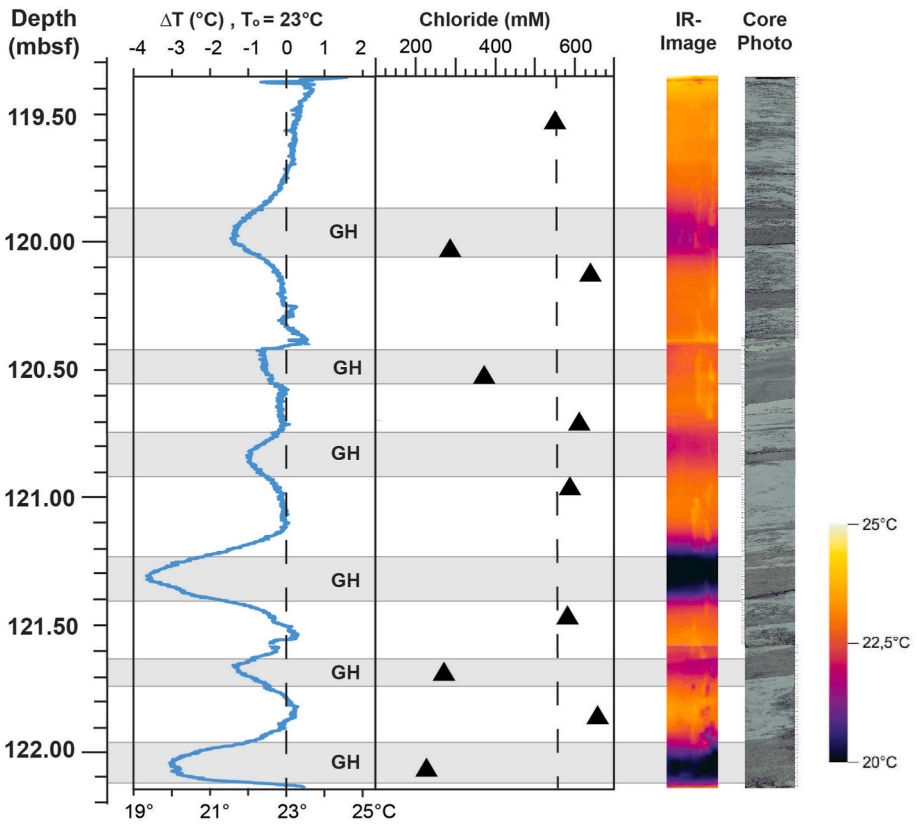

Fig. 9. Correlated data from Core 7R of Hole MeBo-30 at 4WC Ridge (see Fig. 8 for overview): From right to left. Core photograph showing several sandy turbidite layers (dark gray) alternating homogeneous mud (lighter gray), composite infrared images of the core showing cold layers of decomposing hydrates, pore water chloride concentrations and line scan of the temperature distribution with ΔT values (background temperature of 23 °C is assumed; GH = hydrate related cold layer).

than those in the upper section.

The semi-quantitative estimates of hydrate saturation are supported by the resistivity data of the logging measurements. The electrical resistivity of gas hydrate-bearing sediments is higher than that of water-saturated sediments [Tréhu et al., 2003]. In the upper depth interval (13–39 mbsf), the background values of electrical resistivity increase from 1 to 2 Ωm to a maximum of 8 Ωm. In the lower interval with higher methane hydrate saturation, a maximum resistivity of 15 Ωm was reached, and variations of the resistivity curve (Fig. 7) likely reflect fluctuating gas hydrate saturations. Gas hydrate saturation values of 1–10% of the pore space are too low to leave macroscopic traces in the texture of soft carbonate-bearing clay, since the small amount of water released during gas hydrate dissociation does not give a soupy appearance (Fig. 7). It is therefore understandable that no traces of low gas hydrate concentrations can be found in the soft clay lithology (Fig. 7). This is different in the deep gas hydrate-bearing interval with higher hydrate concentrations, where mousse-like and partly soupy textures occur in all sediment cores due to the release of water and free gas during the gas hydrate dissociation (Fig. 7).

Methane concentrations above saturation in pore water are necessary for gas hydrate formation. Biogenic methane is formed by methanogenic archaea from the organic carbon in the sediments, whereby the quality and quantity of the organic matter are key parameters beside sedimentation rate and microbiological activity rates [Davie and Buffett, 2003]. A central question at Formosa Ridge is, why hydrates occur in two specific depth intervals and why there is no evidence for hydrate in the sediments between 39 and 98 mbsf. This observation and the low organic carbon content of 0.3–0.4 wt-% (T. Pape personal communication) in the sediments of Formosa Ridge suggest that the rate of biogenic methane formation was too low to produce significant amounts of hydrate over the entire lengths of the core. Hence, the observed hydrate enrichments may be induced by long-range migration of methane from the surrounding area and below rather than in-situ methane production.

Comparison with reflection seismic data and seafloor observations at the southern summit of Formosa Ridge are important to understand the dynamics and the relationship of free gas and gas hydrate formation in this setting. 60 m north of the boreholes on top of the ridge, where the seafloor is 17 m higher than at the MeBo drill site, gas bubbles are discharged from the seafloor at an individual seepage area (Figs. 1B and 10). Constant emission of free gas was observed by acoustic anomalies in the water column during the drilling. The seepage area is well known since 2007, when it was visited during a Taiwanese-Japanese collaborative cruise with the remotely operated vehicle (ROV) Hyper-Dolphin [Liu et al., 2008]. The seep site is heavily paved by methane-derived carbonates [Feng and Chen, 2015] and in parts densely populated by mytilid bivalves, bacterial mats [Liu et al., 2008] and squat lobsters [Lin et al., 2013; Yang et al., 2016] showing all characteristics of a long-ongoing active seafloor seepage site.

This so-called Formosa Cold Seep, occasionally also called Site F [Feng et al., 2018] is fed through a subsurface fluid conduit, i.e. a complex vertical seismic structure, which is characterized by a disrupted BSR, strong reflectors just above and blanking further up in the vertical extension. This conduit was well imaged during several different seismic surveys (Fig. 3) [Berndt et al., 2019; Hsu et al., 2018; Kunath et al., 2022].

The conduit appears as a vertical zone reaching from several hundreds of meters below the BSR trough the highest point of the BSR [Berndt et al., 2019] allowing free gas to travel several hundreds of meters upwards to the summit, where the Formosa Seep is located. Such conduits are well known from other gas hydrate areas like Vestnesa Ridge [Petersen et al., 2010] and Hydrate Ridge [Crutchley et al., 2013], where increasing pore pressure leads to subsequent hydro-fracturing and vertical fluid flow within the conduit structure [Clennell et al., 2000]. Comprehensive geological and geophysical studies suggest that

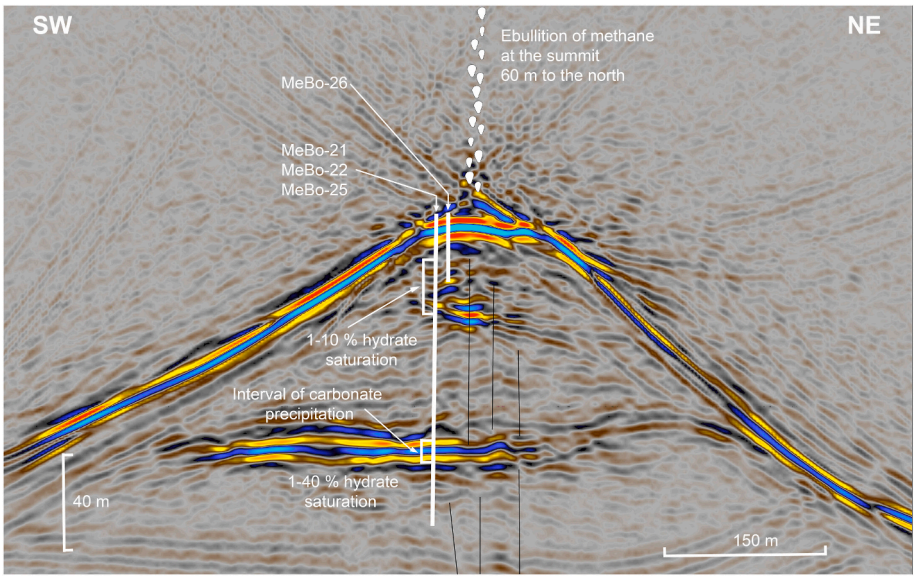

Fig. 10. Main findings in MeBo drillings of gas hydrate distribution at Formosa Ridge and additional information like suspected vertical faults (black lines) and gas bubble ebullition from the summit.

large amounts of free methane can travel upwards in a conduit structure because these systems tend to be out of thermodynamic equilibrium [Crutchley et al., 2013; Smith et al., 2014; Tréhu et al., 2004].

The conduit below Formosa Seep was recently investigated by using high resolution 3D seismic data (Kunath et al., 2022). Episodic venting of gas was postulated from the base of the gas hydrate stability zone below the BSR where gas accumulated up to a critical thickness, causing hydraulic fracturing and propagation of a vertical conduit was interpreted [Kunath et al., 2022]. Methane can form methane hydrate when reaching the hydrate stability zone above the BSR. Former geophysical investigations at Formosa Ridge using controlled source electromagnetic imaging (CSEM) and Ocean-Bottom Seismometer (OBS) measurements implied in general low hydrate saturation ranging between 5% and 10% of the pore space in sediments below Formosa Ridge [Berndt et al., 2019]. Higher saturation values were interpreted at the conduit structure, where electrical resistivity values derived from CSEM are much higher than background values. MeBo drilling on Formosa Ridge near the conduit structure did not reach deeper sediments close to the BSR where the geophysical data predict the highest hydrate saturations.

Nevertheless, the new drilling information of the uppermost 126 mbsf in the vicinity of the conduit are consistent with a highly variable and in some intervals hydrate-bearing setting that would be expected for a conduit structure which is fed by free methane from underneath (Fig. 10). Therefore, it is plausible that the upper interval of gas hydrate-bearing sediments formed due to lateral methane transport from the conduit. High seismic amplitudes are observed between 25 and 40 mbsf in the high-resolution 3D seismic data in the area of the conduit structure.

Although it is not possible to determine the polarity of these arrivals unambiguously due to superposition of several events, the limited lateral extent and the high amplitude suggest that sharp acoustic impedance reduction of free gas causes these reflectors [Berndt et al., 2019]. Free gas was encountered in Hole MeBo-26, 20 m further east of MeBo-21, -22, and -25 and closer to the conduit structure (Fig. 10). Upon reaching a drilling depth of 24 mbsf, ebullition of free gas was so strong that the MeBo drilling system had to be recovered from the borehole (Fig. 10, Table 2). The emanating free gas may have been accumulated in the zone of the seismic anomaly or it may have ascended into the borehole from a greater depth through the conduit structure. Both scenarios seem possible. If free gas is the cause for the high amplitude reflections and is therefore stored in this depth range, then pathways for water must be cut off by gas hydrate formation, because the free gas would form gas hydrate otherwise as the whole system is far inside the gas hydrate stability zone. This suggests that there is a mixture of methane hydrate and free gas in the upper part of Formosa Ridge. This would be similar to the subsurface structures at other cold seep areas, e.g. in pockmarks from the Vestnesa Ridge [Pape et al., 2020a,b] and the Niger deep sea fan [Sultan et al., 2014].

A direct transport of free methane gas from greater depths to the shallow borehole is also conceivable, and would lead to the rapid formation of methane hydrate, at least in the area of the seismic anomaly. Direct ascent of free gas through the gas hydrate stability zone is still enigmatic as it should form hydrate upon encountering free water. Several mechanisms have been proposed to explain this widespread phenomenon ranging from thermodynamic disequilibria to local temperature or salinity anomalies [e.g., Smith et al., 2014], methane gas supply exceeding its consumption by hydrate formation in a high gas flux regime [Liu et al., 2019] to gas hydrate coating the path of the gas ascent, as was observed in the Congo fan region [Pape and Bohrmann, 2022]. In the Congo fan region, numerous gas hydrate tubes were sampled which demonstrate the protective function of gas hydrate rims that separate pore water outside the tube from free gas inside the tube allowing a continuous upward flux of bubble-forming free gas in the interior of the tubes.

Since active free gas transport is occurring in the conduit at least temporarily, the hydrate occurrences encountered in both depth intervals of the Formosa Ridge could be fed by lateral intrusion of light hydrocarbons derived from the conduit. The deeper interval below 98 mbsf with gas hydrate saturation of up to nearly 40% is not accompanied by high amplitude seismic reflections. Intermediate amplitude seismic reflections occur laterally around the conduit structure and approximately 100 m to the Southwest (Fig. 10). Higher amplitude seismic reflections clearly exist above the deep interval of hydrate presence and are correlated with the authigenic carbonate nodules encountered during drilling between 87 and 94 mbsf (Figs. 7 and 10). The seismic reflectors of high amplitudes are continuing horizontally, so that the presence of authigenic carbonates represents a horizontal layer which probably reacts partly as a seal for upwards migrating gas. This seal must have eventually been overcome as now methane is found above this interval and at the seafloor.

However, it can be assumed that the passage of gas through the conduit was at least temporarily blocked for rising free gas at this level.

Gas accumulation below this high reflectivity layers occurred and 1–40% gas hydrate saturation was reached (Fig. 10). The seismic reflections of intermediate amplitudes below 105 mbsf are partially interrupted (Fig. 10), which can be explained by variable gas hydrate concentrations ranging between 1 and 40% of the pore space, meaning that gas hydrates may not form continuous layers. This pattern of distributed small hydrate accumulations, for example along focused fluid flow pathways in sediment deposits was postulated by widespread geophysical investigation of Formosa Ridge in comparison with other hydrate-bearing areas [Berndt et al., 2019] and is consistent with the new drilling results.

The presence of small gas hydrate deposits above the BSR at Formosa Ridge have been postulated based on geophysical investigations [Berndt et al., 2019; Hsu et al., 2018]. Berndt et al., [2019] attribute the chaotic internal sedimentary structures of the ridge to numerous incised and refilled canyons in its northern part and sediment waves in the southern part of the ridge. These sedimentary architectures make it impossible to trace individual layers over large distances. This pattern seems to be typical for other places of the passive margin in the eastern South China Sea. Within a collaborative effort from China, scientists have investigated gas hydrates at several locations of the pasive continental margin, which are part of the Pearl River Mouth Basin [Zhang et al., 2015; Zhang et al., 2020]. Thirteen sites were drilled at the deep slope of the East of Pearl River Mouth Basin in the Horseshoe Ridge and Jiulong Ridge areas [Zhang et al., 2015], 40 and 60 km west of the MeBo drill site on Formosa Ridge (Fig. 1).

Similar to Formosa Ridge, seismic investigations of the Horseshoe and Jiulong Ridges showed widespread high amplitude seismic anomalies, discontinuous BSRs and blanking zones [Zhang et al., 2015]. In addition to disseminated hydrate found at 9–23 mbsf, some massive hydrate samples have been recovered and represent the fracture-filled type of hydrates. In the Formosa Ridge area, gas hydrates at those sites are dominantly composed of biogenic methane. A second area of gas hydrate drilling activities in the South China Sea is the Shenhu area, which is located farther west in the south of the central Pearl River Mouth Basin [Zhang et al., 2020]. Since 2017, the area has become the focus of the offshore gas-hydrate production test, where methane was produced successfully from hydrate reservoirs. This favorable target for large-scale development of gas hydrates was found after extensive exploration during several expeditions in the last decade [Zhang et al., 2020]. In contrast to methane hydrates from Formosa Ridge, Jiulong Ridge and Horseshoe Ridge, higher amounts of thermogenic methane are present in the Shenhu area.

5.2. Gas hydrates at Four-Way Closure Ridge

Gas hydrates are absent from the uppermost 65 m of Holes MeBo-20 and -23 on Four-Way Closure Ridge (Fig. 8). Gas hydrate saturations must be so low that they do not leave any detectable trace in the sediments. This is shown by the very uniform chloride concentrations, which increase continuously from 550 mM near the sediment surface to 570 mM at 65 mbsf, and no anomaly was recognizable (Fig. 8). Between 65 mbsf and 120 mbsf hydrate occurrence is clearly documented by lower chloride concentrations resulting in hydrate saturations ranging between 1 and 20% of pore space (Fig. 8). The sediments are homogeneous clays throughout and there is no change in the sediment composition at a depth of 65 mbsf, i.e. where the change from gas hydrate-free sediments above to gas hydrate-bearing sediments below occurs.

From a depth of 85 mbsf, the fraction of silt/sand increases slightly downward, but even this subtle lithological change does not seem to have a direct effect on the gas hydrate saturation. In Core MeBo-23–28P (approx. 106–109 mbsf), a few pore water samples showing low chloride concentrations suggest an increased hydrate saturation of up to 29%. This is consistent with mousse-like sediment textures at the surface of the core halves (Figs. 6 and 8). None of these weak changes in gas hydrate saturation can be recognized by amplitude changes in the 3D seismic data at the drilling location (Fig. 11).

The pattern is very different for the lowermost 5 m below 120 mbsf. In this lowermost section of Holes MeBo-23 and -30, sand and silt layers are very common, alternating with clay layers. Here, mean gas hydrate saturation values of around 50–60% of pore space sporadically maximizing at up to 80% are observed and correlate with high amplitude reflectors in the 3D seismic data (Fig. 11). Cold spots identified with the IR temperature measurements in MeBo-30 Core 7R (Fig. 9) indicated that all gas hydrate-bearing layers were correlated with sand layers. Unfortunately, not all sand layers were sampled for pore water analysis. On the other hand, all lower chloride concentrations representing gas hydrate occurrence are from sand layers.

The chloride concentrations of the intermediate clay layers range between 578 and 655 mM which are higher than the background concentrations. Enrichment of chlorinity by salt exclusion during hydrate formation in the nearby pore space has been demonstrated in sediments on southern Hydrate Ridge [Haeckel et al., 2004; Torres et al., 2004]. The wide variation in positive concentration anomalies indicates a highly dynamic gas hydrate system and inhibition of rapid diffusive equalization by lithological changes (Fig. 9). The negative chloride anomalies show that the gas hydrate deposits in this depth range are clearly associated with the sand layers, while the clay layers in between do not bear gas hydrates. Sand has a larger pore volume between the sand grains and a higher permeability. This allows gas hydrate crystals to precipitate between the grains and replace water in the inter-granular space of the sand [Weinberger et al., 2005].

Seismic records of Four-Way Closure Ridge show the drilled sand layers with prominent reflections. These are horizontal in the vicinity of the drill site and dip more steeply further east following the plunge of the ridge flank (Fig. 11). Here, the seismic amplitudes are less strong. This change of seismic amplitude may be the result of thinner sand layers or it may in fact represent smaller amounts of gas hydrate at the ridge flank compared to those at the apex of the anticline structure. Methane very likely ascended bedding-parallel along permeable sand layers along the eastern limb and led to the gas hydrate accumulation in the apex area of the anticline. Normal faults from depths underneath the anticlinal ridge may also act as pathways for methane ascent and may have supported the gas hydrate accumulation.

5.3. Sand deposits and its implication for gas hydrate presence

The discovery of sand layers at Four-Way Closure Ridge seems to be highly important for the exploitability of gas hydrate reservoirs in the accretionary wedge. In comparison to hemipelagic mud, such sand layers represent porous reservoirs in which hydrate can concentrate. It has already been proposed that sand layers are more widespread in the accretionary wedge than along the passive continental margin (Fig. 12). This is due to the proximity to the Taiwanese land mass and the existing transport routes [Lin et al., 2014]. The mountain regions of Taiwanese landmasses have very high erosion rates and some of the mountain debris is transported via rivers to the southwest over the continental slope into the deep sea. The main transport is via turbidity-current transport through numerous deeply incised submarine canyons, like Penghu Canyon, Fangliao Canyon, and Kaoping Canyon [Hsiung et al., 2014]. The canyons are formed by the erosive effect of the turbidity currents directed down the slope, whereby there is a clear interaction with the tectonically formed anticlinal ridges in the area of the accretionary wedge. As shown by the bathymetric maps (Fig. 1), the plate tectonic convergence and the subduction geometry cause the formation of accretionary ridges, which are developed roughly parallel to the active margin southwest of Taiwan [e.g., Lin et al., 2008]. Such slope-parallel anticlinal structures form barriers for the turbidity currents directed downhill, whereby they are very often deviated in the direction of the elongated morphological basins between the slope-parallel accretionary ridges and lead to the deposition of sand layers [Hsiung et al., 2014].

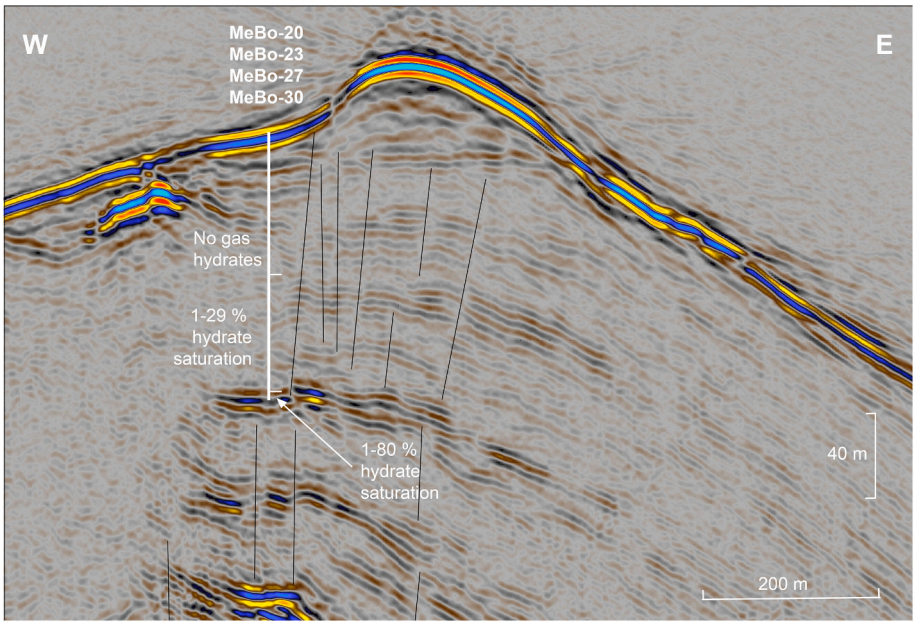

Fig. 11. Hydrate saturation at different depth intervals at MeBo drill sites on Four-Way Closure Ridge (4WC Ridge) and the correlation with seismic data. Suspected vertical faults [Kunath et al., 2022] are shown by black lines.

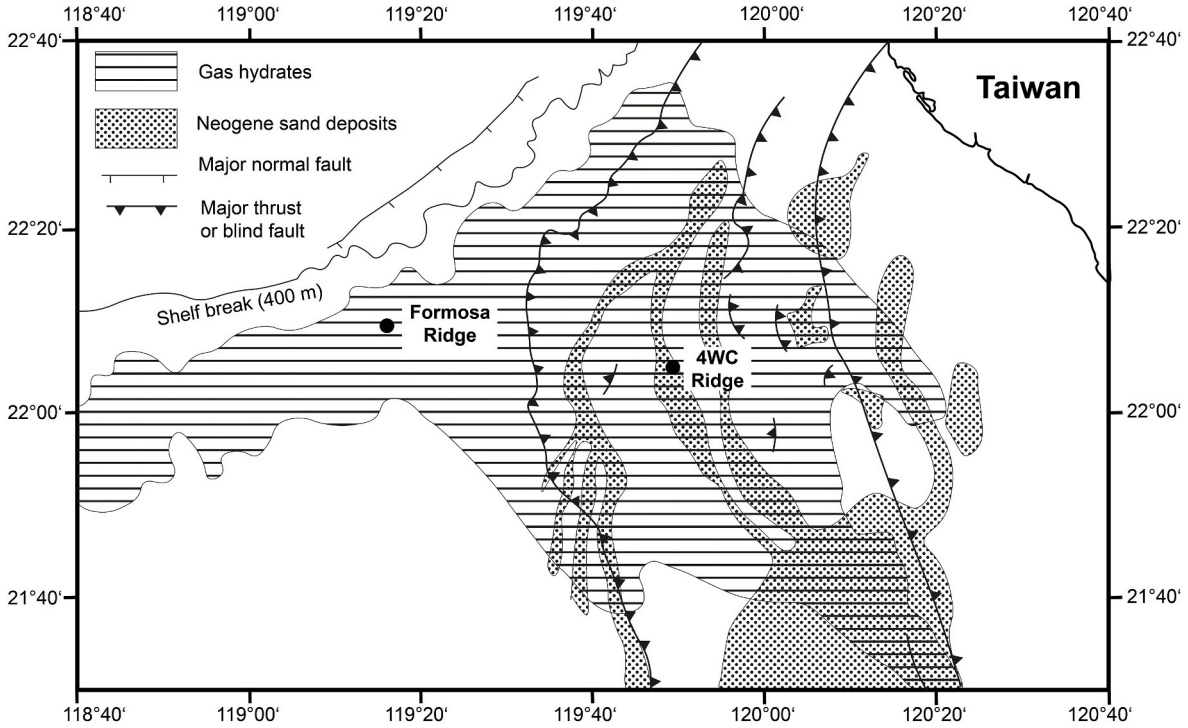

Fig. 12. Tectonic map of the northeastern part of the South China Sea showing the distribution of gas hydrate deposits based on geophysical exploration (Lin et al., 2009; Schnürle et al., 2004] and the occurrence of major sand deposits [Lin et al., 2014]. Positions of both drilling locations, Formosa Ridge at the passive margin and Four-Way Closure Ridge (4WC Ridge) at the accretionary margin SW of Taiwan, are indicated.

The Penghu Canyon is one of those canyons that delivered coarse sediment material downslope to the abyssal plain of the South China Sea, especially during glacial times when the sea level was lower [Lin et al., 2014]. Due to the interaction of the down-slope material transport with the active tectonic evolution of the wedge, the Penghu Canyon has changed its course several times [Lin et al., 2008; Lin et al., 2014] and earlier transport routes led along the eastern and western flanks of the Four-Way Closure Ridge (Fig. 1). The drilled sand layers are result of such a transport in the slope basin between two accretionary anticlinal structures (Fig. 12). The 3D-seismic data for the eastern flank of the Four-Way Closure Ridge (Fig. 2) show a clear unconformity that separates the folded deposits within the ridge from propagating sediments that are filling the slope basin [Kunath et al., 2020].

Layers of coarser clastic sediment components from turbidites are probably well presented in some of the slope valleys as it is shown in Fig. 12. The findings of coarser clastic sediment layers at the base of the

MeBo borehole on Four-Way Closure Ridge show that these sand layers are perfect reservoirs of significant amounts of gas hydrates. Based on the combined analysis of our drilling results with seismic data we postulate large occurrences of gas hydrates within most of the accretionary wedge off Taiwan, which should be confirmed by future drilling.

6. Summary and conclusions

Drilling of the uppermost 136 m sediment deposits both at Formosa Ridge and Four-Way Closure Ridge corroborated to a large extent the inferences that were made based on the analysis of geophysical data. Massive hydrates have not been recovered, but several proxies document the presence and the saturation of gas hydrates offshore southwest of Taiwan. Higher hydrate saturations were more frequently encountered in the active margin at Four-Way Closure Ridge than in the passive margin at Formosa Ridge. In general, hydrate saturations in the shallow subsurface were low, but the drilling data reveal several small-scale gas and gas hydrate occurrences that are beyond the resolution of geophysical data.

Drilling revealed the importance of lithological variations for hydrate saturation. The highest saturations were encountered in sandy turbidites at Four-Way Closure Ridge which is possibly typical for the entire gas hydrate stability zone of the accretionary wedge. The fact, that pore water chlorinity in the clayey interbeds between the sand layers was partly higher than background values suggests that the system is dynamic and at least partly out of thermodynamic equilibrium. This may explain why gas can migrate for considerable distances into the gas hydrate stability zone before forming gas hydrate.

Credit author statement

Gerhard Bohrmann: Conceptualization, Investigation, Writing, Funding acquisition. Christian Berndt: Conceptualization, Investigation, Writing, Funding acquisition. Saulwood Lin: Conceptualization, Investigation, Writing, Funding acquisition. Tzu-Hsuan Tu: Analyses, Text editing. Andrew Tien-Shun Lin: Analyses, Text editing. Ho-Han Hsu: Analyses, Text editing. Mei-Chin Lai: Analyses, Text editing. Wu-Cheng Chi: Analyses, Text editing. Christian Deusner: Analyses, Text editing. Judith Elger: Analyses, Text editing. Klaus Wallmann: Analyses, Text editing. Tim Freudenthal: Analyses, Text editing. Susan Mau: Analyses, Text editing. Thomas Pape: Analyses, Text editing. Yi-Ting Tseng: Analyses, Text editing. Pai-Sen Yu: Analyses, Text editing. Lan-Feng Fan: Analyses, Text editing. Jhen-Nien Chen: Analyses, Text editing. Sheng-Chung Chen: Analyses, Text editing. Tzu-Ting Chen: Analyses, Text editing. Kuo-Yen Wei: Analyses, Text editing.

Declaration of competing interest

The authors declare that they have no known competing financial interests or personal relationships that could have appeared to influence the work reported in this paper.

Data availability

Data are available at the World Data Center PANGAEA (https://www.pangaea.de)

Acknowledgments

R/V SONNE cruise SO266 in Taiwanese waters was planned, coordinated and carried out by MARUM “Center for Marine Environmental Sciences” at the University of Bremen, by GEOMAR Helmholtz Center for Ocean Research in Kiel, and by the Institute of Oceanography, National Taiwan University in Taipei. The cruise was financed in Germany by the Ministry of Education and Science, project TaiDrill – SO266 (Ref. #03G0288A). The project was funded in Taiwan by the Ministry of Science and Technology (MoST) Project TaiGer drill (MOST107-3113-M-002-004). We are grateful to the master of the vessel, Lutz Mallon and his crew and the shipping operator Briese Schiffahrt GmbH & Co. KG for continuous support. We also thank the MeBo team from MARUM and Taiwan Ocean Research Institute (TORI) for their excellent work. Many thanks go to the staff of the German Research Fleet Coordination Center and to the Logistic Department of MARUM as well as to the German Institute in Taipei. We thank the reviewers and the editor for their constructive comments that helped to improve the quality of the manuscript.

References

Berndt, C., Chi, W.-C., Jegen, M., Lebas, E., Crutchley, G., Muff, S., Hölz, S., Sommer, M., Lin, S., Liu, C.-S., Lin, A.T., Klaeschen, D., Klaucke, I., Chen, L., Hsu, H.-H., Kunath, P., Elger, J., McIntosh, K.D., Feseker, T., 2019. Tectonic controls on gas hydrate distribution off SW Taiwan. J. Geophys. Res. Solid Earth 124, 1164–1184. https://doi.org/10.1029/2018jb016213.

Boetius, A., Ravenschlag, K., Schubert, C.J., Rickert, D., Widdel, F., Gieseke, A., Amann, R., Jørgensen, B.B., Witte, U., Pfannkuche, O., 2000. A marine microbial consortium apparently mediating anaerobic oxidation of methane. Nature 407, 623–626. https://doi.org/10.1038/35036572.

Bohrmann, G., Torres, M.E., 2006. Gas hydrates in marine sediments. In: Schulz, H.D., Zabel, M. (Eds.), Marine Geochemistry. Springer, Berlin Heidelberg, pp. 481–512. https://doi.org/10.1007/3-540-32144-6_14.

Bohrmann, G., et al., 2019. MeBo200 methane hydrate drillings southwest of Taiwan (TaiDrill). Cruise No. SO266/1, 15 October –18 November 2018. Kaohsiung (Taiwan) - Kaohsiung. https://doi.org/10.48433/cr_so266_1.

Bowin, C., Lu, R.S., Lee, C.-S., Schouten, H., 1978. Plate convergence and accretion in Taiwan-Luzon Region. AAPG (Am. Assoc. Pet. Geol.) Bull. 62, 1645–1672. https://doi.org/10.1306/c1ea5260-16c9-11d7-8645000102c1865d.

Chen, L., Chi, W.-C., Wu, S.-K., Liu, C.-S., Shyu, C.-T., Wang, Y., Lu, C.-Y., 2014. Two dimensional fluid flow models at two gas hydrate sites offshore southwestern Taiwan. J. Asian Earth Sci. 92, 245–253. https://doi.org/10.1016/j.jseaes.2014.01.004.

Chen, N.-C., Yang, T.F., Hong, W.-L., Chen, H.-W., Chen, H.-C., Hu, C.-Y., Huang, Y.-C., Lin, S., Lin, L.-H., Su, C.-C., Liao, W.-Z., Sun, C.-H., Wang, P.-L., Yang, T., Jiang, S.-Y., Liu, C.-S., Wang, Y., Chung, S.-H., 2017. Production, consumption, and migration of methane in accretionary prism of southwestern Taiwan. G-cubed 18, 2970–2989. https://doi.org/10.1002/2017GC006798.

Chi, W.-C., Reed, D.L., Liu, C.-S., Lundberg, N., 1998. Distribution of the bottom-simulating reflector in the offshore Taiwan collision zone. TAO. Terr. Atmos. Ocean Sci. 9, 779–794. https://doi.org/10.3319/TAO.1998.9.4.779(TAICRUST).

Chiu, J.-K., Wei-Hao, T., Liu, C.-S., 2006. Distribution of gassy sediments and mud volcanoes offshore southwestern Taiwan. TAO. Terr. Atmos. Ocean Sci. 17, 703. https://doi.org/10.3319/TAO.2006.17.4.703(GH).

Chuang, P.-C., Dale, A.W., Wallmann, K., Haeckel, M., Yang, T.F., Chen, N.-C., Chen, H.-C., Chen, H.-W., Lin, S., Sun, C.-H., You, C.-F., Horng, C.-S., Wang, Y., Chung, S.-H., 2013. Relating sulfate and methane dynamics to geology: accretionary prism offshore SW Taiwan. G-cubed 14, 2523–2545. https://doi.org/10.1002/ggge.20168.

Chuang, P.-C., Yang, T.F., Hong, W.-L., Lin, S., Sun, C.-H., Lin, A.T.-S., Chen, J.-C., Wang, Y., Chung, S.-H., 2010. Estimation of methane flux offshore SW Taiwan and the influence of tectonics on gas hydrate accumulation. Geofluids 10, 497–510. https://doi.org/10.1111/j.1468-8123.2010.00313.x.

Clennell, M.B., Judd, A., Hovland, M., 2000. Movement and accumulation of methane in marine sediments: relation to gas hydrate systems. In: Max, M.D. (Ed.), Natural Gas Hydrate in Oceanic and Permafrost Environments. Kluwer Academic Publ, Dordrecht, pp. 105–122. https://doi.org/10.1007/978-94-011-4387-5_9.

Collett, T., Riedel, M., Cochran, J.R., Boswell, R., Kumar, P., Sathe, A., 2008. Indian continental margin gas hydrate prospects: results of the Indian National Gas Hydrate Program (NGHP) expedition 01. In: Proceedings of the 6th International Conference on Gas Hydrates (ICGH 2008). Vancouver, British Columbia, Canada.

Crutchley, G.J., Berndt, C., Geiger, S., Klaeschen, D., Papenberg, C., Klaucke, I., Hornbach, M.J., Bangs, N.L.B., Maier, C., 2013. Drivers of focused fluid flow and methane seepage at south Hydrate Ridge. offshore Oregon, USA. Geology 41, 551–554. https://doi.org/10.1130/g34057.1.

Davie, M.K., Buffett, B.A., 2003. Sources of methane for marine gas hydrate: inferences from a comparison of observations and numerical models. Earth Planet Sci. Lett. 206, 51–63. https://doi.org/10.1016/S0012-821X(02)01064-6.

Dickens, G.R., 2003. Rethinking the global carbon cycle with a large, dynamic and microbially mediated gas hydrate capacitor. Earth Planet Sci. Lett. 213, 169–183. https://doi.org/10.1016/S0012-821X(03)00325-X.

Feng, D., Chen, D., 2015. Authigenic carbonates from an active cold seep of the northern South China Sea: new insights into fluid sources and past seepage activity. Deep-Sea Res. Part II 122, 74–83. https://doi.org/10.1016/j.dsr2.2015.02.003.

Feng, D., Qiu, J.-W., Hu, Y., Peckmann, J., Guan, H., Tong, H., Chen, C., Chen, J., Gong, S., Li, N., Chen, D., 2018. Cold seep systems in the South China Sea: An overview. J. Asian Earth Sci. 168, 3–16. https://doi.org/10.1016/j.jseaes.2018.09.021.

Freudenthal, T., Wefer, G., 2013. Drilling cores on the sea floor with the remote-controlled sea floor drilling rig MeBo. Geosci. Instrum. Method. Data Syst. 2, 329–337. https://doi.org/10.5194/gi-2-329-2013.

Fujii, T., Saeki, T., Kobayashi, T., Inamori, T., Hayashi, M., Takano, O., Takayama, T., Kawasaki, T., Nagakubo, S., Nakamizu, M., 2008. Resource assessment of methane hydrate in the Eastern Nankai Trough, Japan. Offshore Technology Conference. OnePetro. OTC-19310-M.. https://doi.org/10.4043/19310-MS.

Haeckel, M., Suess, E., Wallmann, K., Rickert, D., 2004. Rising methane gas bubbles form massive hydrate layers at the seafloor. Geochem. Cosmochim. Acta 68, 4335–4345. https://doi.org/10.1016/j.gca.2004.01.018.

Himmler, T., Sahy, D., Martma, T., Bohrmann, G., Plaza-Faverola, A., Bünz, S., Condon, D.J., Knies, J., Lepland, A., 2019. A 160,000-year-old history of tectonically controlled methane seepage in the Arctic. Sci. Adv. 5, eaaw1450.. https://doi.org/10.1126/sciadv.aaw1450.

Hong, W.L., Pape, T., Schmidt, C., Yao, H., Wallmann, K., Plaza-Faverola, A., Rae, J.W.B., Lepland, A., Bünz, S., Bohrmann, G., 2021. Interactions between deep formation fluid and gas hydrate dynamics inferred from pore fluid geochemistry at active pockmarks of the Vestnesa Ridge, west Svalbard margin. Mar. Petrol. Geol. 127, 104957 https://doi.org/10.1016/j.marpetgeo.2021.104957.

Hsiung, K.-H., Yu, H.-S., Chiang, C.-S., 2014. Seismic characteristics, morphology and formation of the ponded Fangliao Fan off southwestern Taiwan, northern South China Sea. Geo Mar. Lett. 34, 59–74. https://doi.org/10.1007/s00367-013-0351-1.

Hsu, H.-H., Liu, C.-S., Morita, S., Tu, S.-L., Lin, S., Machiyama, H., Azuma, W., Ku, C.-Y., Chen, S.-C., 2018. Seismic imaging of the Formosa Ridge cold seep site offshore of southwestern Taiwan. Mar. Geophys. Res. 39, 523–535. https://doi.org/10.1007/s11001-017-9339-y.

Huang, Y.-S., Hsu, S.-K., Su, C.-C., Lin, A.T.-S., Yu, P.-S., Babonneau, N., Ratzov, G., Lallemand, S., Huang, P.-C., Lin, S.-S., Lin, J.-Y., Wei, K.-Y., Chang, Y.-P., Yu, N.-T., Tsai, C.-H., 2021. Shallow gas hydrates off southwest Taiwan and their mechanisms. Mar. Geophys. Res. 42, 7. https://doi.org/10.1007/s11001-021-09429-x.

Kastner, M., Elderfield, H., Martin, J.B., 1991. Fluids in convergent margins: what do we know about their composition, origin, role in diagenesis and importance for oceanic chemical fluxes. Phil. Trans. Roy. Soc. Lond. 335, 243–259. https://doi.org/10.1098/rsta.1991.0045.

Kim, J.-H., Torres, M.E., Hong, W.-L., Choi, J., Riedel, M., Bahk, J.-J., Kim, S.-H., 2013. Pore fluid chemistry from the Second Gas Hydrate Drilling Expedition in the Ulleung Basin (UBGH2): Source, mechanisms and consequences of fluid freshening in the central part of the Ulleung Basin, East Sea. Mar. Petrol. Geol. 47, 99–112. https://doi.org/10.1016/j.marpetgeo.2012.12.011.

Klaucke, I., Berndt, C., Crutchley, G., Chi, W.-C., Lin, S., Muff, S., 2016. Fluid venting and seepage at accretionary ridges: the Four Way Closure Ridge offshore SW Taiwan. Geo Mar. Lett. 36, 165–174. https://doi.org/10.1007/s00367-015-0431-5.

Kück, J., Groh, M., Töpfer, M., Jurczyk, A., Harms, U., 2021. New geophysical memory-logging system for highly unstable and inclined scientific exploration drilling. Sci. Drill. 29, 39–48. https://doi.org/10.5194/sd-29-39-2021.

Kunath, P., Chi, W.-C., Berndt, C., Chen, L., Liu, C.-S., Kläschen, D., Muff, S., 2020. A shallow seabed dynamic gas hydrate system off SW Taiwan: Results from 3-D seismic, thermal, and fluid migration analyses. J. Geophys. Res. Solid Earth 125, e2019JB019245-T. https://doi.org/10.1029/2019JB019245.

Kunath, P., Crutchley, G., Chi, W.C., Berndt, C., Liu, C.S., Elger, J., Klaeschen, D., Bohrmann, G., 2022. Episodic venting of a submarine gas seep on geological time scales: Formosa Ridge, northern South China Sea. J. Geophys. Res. Solid Earth 127, e2022JB024668. https://doi.org/10.1029/2022JB024668.

Kvenvolden, K.A., 1988. Methane hydrate - A major reservoir of carbon in the shallow geosphere? Chem. Geol. 71, 41–51. https://doi.org/10.1016/0009-2541(88)90104-0.

Kvenvolden, K.A., 1998. A primer on the geological occurrence of gas hydrate. In: Henriet, J.P., Mienert, J. (Eds.), Gas Hydrates: Relevance to World Margin Stability and Climate Change. Geological Society, London, pp. 9–30. https://doi.org/10.1144/GSL.SP.1998.137.01.02.

Kvenvolden, K.A., Lorenson, T.D., 2001. The global occurrence of natural gas hydrates. In: Paull, C. (Ed.), Natural Gas Hydrates: Occurrence, Distribution, and Detection. American Geophysical Union, pp. 3–18. https://doi.org/10.1029/GM124p0003.

Li, J.-F., Ye, J.-L., Qin, X.-W., Qiu, H.-J., Wu, N.-Y., Lu, H.-L., Xie, W.-W., Lu, J.-A., Peng, F., Xu, Z.-Q., Lu, C., Kuang, Z.-G., Wei, J.-G., Liang, Q.-Y., Lu, H.-F., Kou, B.-B., 2018. The first offshore natural gas hydrate production test in South China Sea. China Geology 1, 5–16. https://doi.org/10.31035/cg2018003.

Lin, A.T., Liu, C.-S., Lin, C.-C., Schnurle, P., Chen, G.-Y., Liao, W.-Z., Teng, L.S., Chuang, H.-J., Wu, M.-S., 2008. Tectonic features associated with the overriding of an accretionary wedge on top of a rifted continental margin: an example from Taiwan. Mar. Geol. 255, 186–203. https://doi.org/10.1016/j.margeo.2008.10.002.

Lin, C.-W., Tsuchida, S., Lin, S., Berndt, C., Chan, T.-Y., 2013. *Munidopsis lauensis* Baba & de Saint Laurent, 1992 (Decapoda, Anomura, Munidopsidae), a newly recorded squat lobster from a cold seep in Taiwan. Zootaxa 3737, 92–96.

Lin, A.T., Yao, B., Hsu, S.-K., Liu, C.-S., Huang, C.-Y., 2009. Tectonic features of the incipient arc-continent collision zone of Taiwan: implications for seismicity. Tectonophysics 479, 28–42. https://doi.org/10.1016/j.tecto.2008.11.004.

Lin, C.-C., Lin, A.T.-S., Liu, C.-S., Horng, C.-S., Chen, G.-Y., Wang, Y., 2014. Canyon-infilling and gas hydrate occurrences in the frontal fold of the offshore accretionary wedge off southern Taiwan. Mar. Geophys. Res. 35, 21–35. https://doi.org/10.1007/s11001-013-9203-7.

Liu, J., Haeckel, M., Rutqvist, J., Wang, S., Yan, W., 2019. The mechanism of methane gas migration through the gas hydrate stability zone: insights from numerical simulations. J. Geophys. Res. Solid Earth 124, 4399–4427. https://doi.org/10.1029/2019JB017417.

Liu, C.-S., Morita, S., Liao, Y.-H., Ku, C.-Y., Machiyama, H., Lin, S., Soh, W., 2008. High-resolution seismic images of the Formosa Ridge off Southwestern Taiwan where "hydrothermal" chemosynthetic community is present at a cold seep site. In: Proceedings of the 6th International Conference on Gas Hydrates (ICGH 2008). Vancouver, British Columbia, Canada.

Liu, C.-S., Schnurle, P., Wang, Y., San-Hsiung, C., Song-Chuen, C., Hsiuan, T.-H., 2006. Distribution and characters of gas hydrate offshore of southwestern Taiwan. TAO. Terr. Atmos. Ocean Sci. 17, 615. https://doi.org/10.3319/TAO.2006.17.4.615(GH).

Pape, T., Bohrmann, G., 2022. Shallow gas hydrates associated to pockmarks in the Northern Congo deep-sea fan, SW Africa. In: Mienert, J., Berndt, C., Tréhu, A.M., Camerlenghi, A., Liu, C.-S. (Eds.), World Atlas of Submarine Gas Hydrates in Continental Margins, first ed. Springer, Cham, pp. 359–371. https://doi.org/10.1007/978-3-030-81186-0_31.

Pape, T., Bünz, S., Hong, W.-L., Torres, M.E., Riedel, M., Panieri, G., Lepland, A., Hsu, C.-W., Wintersteller, P., Wallmann, K., Schmidt, C., Yao, H., Bohrmann, G., 2020a. Origin and transformation of light hydrocarbons ascending at an active pockmark on Vestnesa Ridge, Arctic Ocean. J. Geophys. Res. Solid Earth 125, e2018JB016679. https://doi.org/10.1029/2018jb016679.

Pape, T., Ruffine, L., Hong, W.-L., Sultan, N., Riboulot, V., Peters, C.A., Kölling, M., Zabel, M., Garziglia, S., Bohrmann, G., 2020b. Shallow gas hydrate accumulations at a Nigerian deepwater pockmark—quantities and dynamics. J. Geophys. Res. Solid Earth 125, e2019JB018283. https://doi.org/10.1029/2019jb018283.

Paull, C., Bohrmann, G., Brewer, P., Cochanat, P., Collett, T., Edwards, N., Hovland, M., Johnson, A., Kvenvolden, K., Matsumoto, R., Sloan, D., Tréhu, A., Westbrook, G., 2000a. Excerpts from the final report of JOIDES gas hydrate program planning group. JOIDES Journal 26, 33–39.

Paull, C.K., Matsumoto, R., Wallace, P.J., Dillon, W.P., 2000b. Proceedings of the Ocean Drilling Program 164, Scientific Results. Ocean Drilling Program, College Station TX. https://doi.org/10.2973/odp.proc.sr.164.2000.

Petersen, C.J., Bünz, S., Hustoft, S., Mienert, J., Klaeschen, D., 2010. High-resolution P-Cable 3D seismic imaging of gas chimney structures in gas hydrated sediments of an Arctic sediment drift. Mar. Petrol. Geol. 27, 1981–1994. https://doi.org/10.1016/j.marpetgeo.2010.06.006.

Reed, D., Lundberg, N., Liu, C.-S., Kuo, B.-Y., 1992. Structural relations along the margins of the offshore Taiwan accretionary wedge: implications for accretion and crustal kinematics, Yánjiū bàogào-Guóli Táiwān dàxué. Lǐxuéyuàn dìzhìxué xì=Acta Geologica Taiwanica 30, 105–122.

Riedel, M., Collett, T., Malone, M., Akiba, F., Blanc-Valleron, M., Ellis, M., Guerin, G., Hashimoto, Y., Heuer, V., Higashi, Y., Holland, M., Jackson, P., Kaneko, M., Kastner, M., Kim, J.-H., Kitajima, H., Long, P., Malinverno, A., Myers, G., Palekar, L., Pohlman, J., Schultheiss, P., Teichert, B., Torres, M., Tréhu, A., Wang, J., Wortmann, U., Yoshioka, H., 2006. Gas hydrate transect across Northern Cascadia Margin. Eos, Transactions American Geophysical Union 87, 325–332. https://doi.org/10.1029/2006eo330002.

Ruppel, C.D., Waite, W.F., 2020. Timescales and processes of methane hydrate formation and breakdown, with application to geologic systems. J. Geophys. Res. Solid Earth 125, e2018JB016459. https://doi.org/10.1029/2018JB016459.

Schnurle, P., Liu, C.-S., Hsiuan, T.-H., Wang, T.-K., 2004. Characteristics of gas hydrate and free gas offshore southwestern Taiwan from a combined MCS/OBS data analysis. Mar. Geophys. Res. 25, 157–180. https://doi.org/10.1007/s11001-005-0740-6.

Schnürle, P., Liu, C.-S., Lin, A.T., Lin, S., 2011. Structural controls on the formation of BSR over a diapiric anticline from a dense MCS survey offshore southwestern Taiwan. Mar. Petrol. Geol. 28, 1932–1942. https://doi.org/10.1016/j.marpetgeo.2010.12.004.

Seno, T., Stein, S., Gripp, A.E., 1993. A model for the motion of the Philippine Sea Plate consistent with NUVEL-1 and geological data. J. Geophys. Res. Solid Earth 98, 17941–17948. https://doi.org/10.1029/93JB00782.

Shipley, T.H., Houston, M.H., Buffler, R.T., Shaub, F.J., McMillen, K.J., Ladd, J.W., Worzel, J.L., 1979. Seismic evidence for widespread possible gas hydrate horizons on continetal slopes and rises. AAPG (Am. Assoc. Pet. Geol.) Bull. 63, 2204–2213. https://doi.org/10.1306/2f91890a-16ce-11d7-8645000102c1865d.

Sloan, E.D., Koh, C.A., 2008. Clathrate Hydrates of Natural Gases - Chemical Industries, third ed. CRC Press, Taylor & Francis Group, Boca Raton - London - New York.

Smith, A.J., Flemings, P.B., Liu, X., Darnell, K., 2014. The evolution of methane vents that pierce the hydrate stability zone in the world's oceans. J. Geophys. Res. Solid Earth 119, 6337–6356. https://doi.org/10.1002/2013jb010686.

Sultan, N., Bohrmann, G., Ruffine, L., Pape, T., Riboulot, V., Colliat, J.L., De Prunelé, A., Dennielou, B., Garziglia, S., Himmler, T., Marsset, T., Peters, C.A., Rabiu, A., Wei, J., 2014. Pockmark formation and evolution in deep water Nigeria: Rapid hydrate growth versus slow hydrate dissolution. J. Geophys. Res. Solid Earth 119, 2679–2694. https://doi.org/10.1002/2013JB010546.

Takeya, S., Uchida, T., Nagao, J., Ohmura, R., Shimada, W., Kamata, Y., Ebinuma, T., Narita, H., 2005. Particle size effect of CH_4 hydrate for self-preservation. Chem. Eng. Sci. 60, 1383–1387. https://doi.org/10.1016/j.ces.2004.10.011.

Torres, M.E., Wallmann, K., Tréhu, A.M., Bohrmann, G., Borowski, W.S., Tomaru, H., 2004. Gas hydrate growth, methane transport, and chloride enrichment at the southern summit of Hydrate Ridge, Cascadia margin off Oregon. Earth Planet Sci. Lett. 226, 225–241. https://doi.org/10.1016/j.epsl.2004.07.029.

Tréhu, A.M., Bohrmann, G., Rack, F.R., Torres, M.E., Leg 204 scientific party, 2003. Drilling gas hydrates on Hydrate Ridge, Cascadia continental margin. ODP Inital Report 204. https://doi.org/10.2973/odp.proc.ir.204.2003.

Tréhu, A.M., Long, P.E., Torres, M.E., Bohrmann, G., Rack, F.R., Collett, T.S., Goldberg, D.S., Milkov, A.V., Riedel, M., Schultheiss, P., Bangs, N.L., Barr, S.R., Borowski, W.S., Claypool, G.E., Delwiche, M.E., Dickens, G.R., Gracia, E., Guerin, G., Holland, M., Johnson, J.E., Lee, Y.J., Liu, C.S., Su, X., Teichert, B., Tomaru, H., Vanneste, M., Watanabe, M., Weinberger, J.L., 2004. Three-dimensional distribution of gas hydrate beneath southern Hydrate Ridge: constraints from ODP Leg 204. Earth Planet Sci. Lett. 222, 845–862. https://doi.org/10.1016/j.epsl.2004.03.035.

Tréhu, A.M., Torres, M.E., Bohrmann, G., Colwell, F., 2006. Leg 204 synthesis: gas hydrate distribution and dynamics in the central Cascadia accretionary complex. In: Tréhu, A.M., Bohrmann, G., Torres, M.E., Colwell, F.S. (Eds.), pp. 1–40. https://doi.org/10.2973/odp.proc.sr.204.101.2006. College Station, TX.

Tseng, Y., Römer, M., Lin, S., Pape, T., Berndt, C., Chen, T.-T., Paull, C.K., Caress, D.W., Bohrmann, G., 2023. Yam Seep at Four-Way Closure Ridge: a prominent active gas seep system at the accretionary wedge SW offshore Taiwan. International Journal of Earth Sciences 112, 1043–1061. https://doi.org/10.1007/s00531-022-02280-4.

Ussler, W., III, Paull, C.K., 2001. Ion exclusion associated with marine gas hydrate deposits. In: Paull, C.K., Dillon, W.P. (Eds.), Natural Gas Hydrate: Occurrence, Distribution, and Detection. The American Geophysical Union, Washington D.C., pp. 41–51. https://doi.org/10.1029/GM124p0041.

Weinberger, J.L., Brown, K.M., Long, P.E., 2005. Painting a picture of gas hydrate distribution with thermal images. Geophys. Res. Lett. 32, L04609 https://doi.org/10.1029/2004gl021437.

Yang, C.-H., Tsuchida, S., Fujikura, K., Fujiwara, Y., Kawato, M., Chan, T.-Y., 2016. Connectivity of the squat lobsters *Shinkaia crosnieri* (Crustacea: Decapoda: galatheidae) between cold seep and hydrothermal vent habitats. Bull. Mar. Sci. 92, 17–31. https://doi.org/10.5343/bms.2015.1031.

Zhang, G., Liang, J., Lu, J.a., Yang, S., Zhang, M., Holland, M., Schultheiss, P., Su, X., Sha, Z., Xu, H., Gong, Y., Fu, S., Wang, L., Kuang, Z., 2015. Geological features, controlling factors and potential prospects of the gas hydrate occurrence in the east part of the Pearl River Mouth Basin, South China Sea. Mar. Petrol. Geol. 67, 356–367. https://doi.org/10.1016/j.marpetgeo.2015.05.021.

Zhang, W., Liang, J., Wei, J., Lu, J.a., Su, P., Lin, L., Huang, W., Guo, Y., Deng, W., Yang, X., Wan, Z., 2020. Geological and geophysical features of and controls on occurrence and accumulation of gas hydrates in the first offshore gas-hydrate production test region in the Shenhu area, Northern South China Sea. Mar. Petrol. Geol. 114, 104191 https://doi.org/10.1016/j.marpetgeo.2019.104191.

Data bank storage

Freudenthal, Tim, 2020. Spectrum gamma ray borehole logging data of MeBo sediment core GeoB23213-1. PANGAEA. https://doi.org/10.1594/PANGAEA.914594.

Freudenthal, Tim, 2020. Spectrum gamma ray borehole logging data of MeBo sediment core GeoB23227-1. PANGAEA. https://doi.org/10.1594/PANGAEA.914595.

Freudenthal, Tim, 2020. Resistivity RDeep and RMedium borehole logging data of MeBo sediment core GeoB23227-1. PANGAEA. https://doi.org/10.1594/PANGAEA.914584.

Lin, Saulwood, Bohrmann, Gerhard, 2022. Chloride concentrations and calculated gas hydrate saturations in sediments collected at Formosa Ridge, RV Sonne cruise SO266/1, South China Sea. PANGAEA. https://doi.org/10.1594/PANGAEA.953067.

Lin, Saulwood, Bohrmann, Gerhard, 2022. Chloride concentrations and calculated gas hydrate saturations in sediments collected at Four-Way Closure Ridge, RV Sonne cruise SO266/1, South China Sea. PANGAEA https://doi.pangaea.de/10.1594/PANGAEA.953069.

Bohrmann, Gerhard, 2022. Carbonate contents in sediments collected at Formosa Ridge, RV Sonne cruise SO266/1, South China Sea. PANGAEA https://doi.pangaea.de/10.1594/PANGAEA.952945.

Bohrmann, Gerhard, 2022. Carbonate contents in sediments collected at Four-Way Closure Ridge, RV Sonne cruise SO266/1, South China Sea. PANGAEA https://doi.pangaea.de/10.1594/PANGAEA.952947.